J. Fluid Mech. (1995), *vol.* 287, *pp.* 349–382

Mechanics of collisional motion of granular materials. Part 2. Wave propagation through vibrofluidized granular layers

By ALEXANDER GOLDSHTEIN, MICHAEL SHAPIRO†, LEONID MOLDAVSKY AND MATI FICHMAN

Faculty of Mechanical Engineering, Technion – Israel Institute of Technology, Haifa 32000, Israel

(Received 2 September 1993 and in revised form 2 November 1994)

According to numerous experimental observations and theoretical models vibrated layers composed of large granules behave like a solid plastic body. In contrast, in this study experimental data are presented that reveal that, for constant vibration amplitudes $A \geqslant 1$ cm with the frequency ω increasing from zero, all layers pass through three vibrational states, with the respective behaviours being as of (i) a solid plastic body, (ii) a liquid, (iii) a gas. In the liquid-like vibrational state transverse waves propagating along the layer width were observed. These waves were shown to be gravitational resonance waves, with the corresponding frequencies well correlated by the known formula for incompressible liquids. In the gas-like vibrational state compression (shock) and expansion waves propagating across the layer height, were observed.

A theoretical model for time-periodic collisional vibrational regimes was developed on the basis of the Euler-like equations of a granular gas composed of inelastic spheres. The model shows that the vibrational granular state (bed porosity, shock wave speed, granular pressure and kinetic energy) is *inter alia* governed by the dimensionless parameter $V = (A\omega)/(h_m g)^{1/2}$, with g, h_m being the gravitational acceleration and the height of the resting layer, respectively. This is in contrast with the previous studies, where the behaviour of vibrated granular layers was interpreted in terms of the dimensionless acceleration $\Gamma = (A\omega^2)/g$. The proposed model was tested by processing the data obtained from photographs of the particle distribution within vibrated layers. Theoretical predictions of the particle average concentration compared favourably with the experimental data.

Other phenomena observed in vibrated granular layers include the formation of caverns, circulatory motion of granules and synchronized periodic motion of two adjacent vibrated layers of different widths. The importance of the observed phenomena in relation to various technological processes involving bulk materials (vibromixing, vibroseparation, etc.) is discussed.

1. Introduction

Moving granular materials are widely met in Nature and in various industrial technological processes. Examples include particle conveying (Erdèsz & Nèmeth 1988), classification, separation, mixing, discharge and drying, as well as heat transfer processes (Chlenov & Mikhailov 1972; Gutman 1968; Roberts 1984). The motion of

† To whom all correspondence should be addressed.

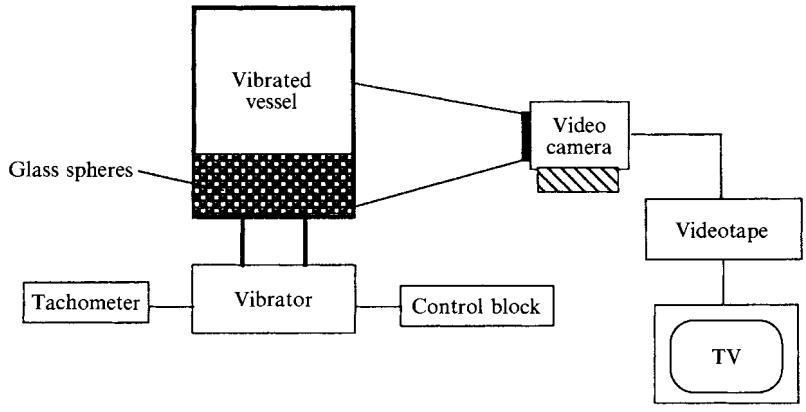

FIGURE 1. Schematic diagram of experimental apparatus.

granular media may occur in several regimes, which can be subdivided into rapid and slow flows. The latter flows are characterized by permanent contacts between neighbouring particles during their motion. In these regimes bulk properties of moving granular media are controlled by the Coulomb interparticle friction forces. On the other hand, in rapid flows particles interact by fast impacts when they collide. Most of the time particles are freely flying between successive collisions, during which the particle kinetic energy and momentum are transferred. Particle impacts within granular media are accompanied by kinetic energy losses associated with the non-conservative nature of these interactions. The effect of these losses is to increase the particles' internal energy, and, hence, their temperature. Therefore, a constant source of mechanical energy is needed to sustain the collisional motion.

Rapid granular flows may be classified with respect to the nature of external energy sources supplying kinetic energy to moving particles. These sources include (i) gravity force, which, in particular, causes rapid shear flows of granular materials on inclined surfaces; (ii) air pressure, which governs particle motion in pneumotransport, fluidized beds, etc.; (iii) externally applied electric or magnetic fields (e.g. in electro- and magnetofluidized beds); (iv) externally induced vibrations. The latter motion includes applications in vibromixing, vibroseparation and vibrofluidization processes (Chlenov & Mikhailov 1972; Gutman 1968; Roberts 1984) and vibrational enhancement of catalytic processes (Thomas & Squires 1989). This study is concerned with the collisional motion coerced by externally applied vibrations.

The behaviour of granular materials moving in collisional regimes is similar to that of flowing liquids or gases. This was experimentally observed for rapid shear flows (see the review by Savage 1984) and for granular materials excited by external vibrations (Chlenov & Mikhailov 1972). When vibrated, granular materials fill vessels of arbitrary forms. Moreover, experiments performed by Chlenov & Mikhailov show that vibrofluidized granular layers subjected to small simple shear rates $\gamma = \mathrm{d}u/\mathrm{d}y$ behave like Stokesian viscous fluids, i.e. shear stresses arising within the layers are proportional to γ.

The collisional motion of granular media may be investigated by stochastic analyses of ensembles of identical (in most cases spherical or disk-like) particles, possessing specified inelasticity and roughness. These particle properties appear in the various collisional models used to describe the collisional motion of granular media by (coarse-scale) hydrodynamic equations. The effective transport properties required in these equations are obtained by various averaging methods. Specific studies dealing with

stochastic analyses of moving granular materials were concerned with modelling of fluidized (Nigmatullin 1978; Homsy, Jackson & Grace 1992), magneto-fluidized (Buevich, Sutkin & Tetukhin 1984), and rapid granular flows (Campbell 1990). The latter problem has received wide attention in the literature and has been treated by various methods of different rigour and complexity. The collisional motion of vibrofluidized granular materials has not been yet analysed, although it may be inferred that it may also be modelled by appropriate hydrodynamic equations (Raskin 1975; Haff 1983).

Fluidized collisional states in vibrated granular layers result from conversion of the work performed by the vessel, E_w, into the kinetic energy, E, of random granular motion. The mechanism responsible for the transformation of E_w into E in vibrofluidized layers (as well as in molecular gases) is provided by compression waves (Goldshtein & Shapiro 1995). Compression and expansion waves are, therefore, phenomena inherent in the vibrofluidization of granular materials. Experimental observation and modelling of these wavy processes occurring during collisional motion of vibrated granular materials are the objectives of the present work.

The first attempt to treat the collisional motion of vibrational granular layers by means of a hydrodynamic model was made by Savage (1988). He assumed the existence of 'acoustic waves' leading to 'acoustic streaming' (similar to the comparable phenomena in viscous fluids), when trying to explain the appearance of circulatory streams within vibrofluidized dry granular materials. However, no wavy motion had yet been seen in vibrofluidized layers of large heavy granules. The phenomena observed so far in such layers included particle convective motion and segregation of particles of different sizes (see the recent review by Meakin & Skjeltorp 1993).

Bachmann (1940) found that vibrated beds of large lead and glass spheres act as a single block when the bed depth exceeds about six particle monolayers. These observations led to modelling vibrated bed behaviour as a single perfectly plastic body (single-body model) (Kroll 1954; Gutman 1976). A liquid-like behaviour was found in the upper parts of vibrated layers thicker than about six particle monolayers (Clement & Rajchenbach 1991). Bending of vibrated beds of small particles (powders) was observed by Thomas *et al.* (1987) and Fauve, Douady & Laroshe (1989). This can largely be attributed to the effect of particle–air interactions dominating the motion of small particles.

All previous experimental investigations (Kroll 1954; Gutman 1976; Thomas *et al.* 1987, 1989) were conducted for vibration frequencies, f, of 25–150 Hz, with a maximum acceleration of g–$10g$. These regimes were chosen for investigation because of the typical features of vibrating mechanical equipment, e.g. electromagnetic vibrators, and also because of the single-body model, generally accepted for the description of the vibrational motion of bulk materials. According to the concepts of solid mechanics (Kroll 1954; Gutman 1976; Erdèsz & Mujumdar 1989) the motion of a rigid body is governed by the gravitational force mg, and the inertial force $m\omega^2 A$ induced by the vibrating vessel, with m being the particle mass; A and $\omega = 2\pi f$ being the amplitude and the angular frequency of vibrations, respectively. As such, the ratio $\Gamma = A\omega^2/g$ serves as the single dimensionless parameter governing the rigid-body motion of a granular material. Since modern vibrational stands generate vibrations with relatively small amplitudes (several millimetres), in all experiments the parameter Γ was varied by means of an appropriate choice of the frequency f within the range of 25–150 Hz.

How can collisional regimes be achieved in vibrofluidized granular layers? It is clear that in all experiments on vibrofluidized layers the kinetic energy of the moving wall,

E_w, was mainly transformed into the kinetic energy associated with the *average* motion of the whole layer, rather than to the kinetic energy, E, of random granular motion. As a result, layers behaved like single bodies, i.e. the granular kinetic energy remained low.

In order to observe the propagation of compression waves the layer compressibility should be increased, which means that sufficiently low particle number densities need to be achieved. Therefore, in these regimes granular kinetic energy should be increased. It is well known (Courant & Friedrichs 1948) that a wall moving with a velocity v generates gas kinetic energy of the order v^2. As such, in order to increase the granular kinetic energy and, hence, the layer compressibility, the wall's maximum vibrational velocity $u_{max} = A\omega$ should be increased.

In the above studies $A\omega$ was small, therefore the compressibility of the granular layers was negligible and no waves could be observed. Indeed, since in all these studies the layers were vibrated with small amplitudes A, large vibrational velocities $A\omega$ could be achieved only by increasing the frequency ω. However, any significant increase of ω is clearly accompanied by rapidly increasing acceleration $A\omega^2$, which is limited by the strength requirements.

Bearing in mind the above considerations, in the present study granular layers are experimentally investigated with large vibrational velocities $A\omega$, which is achieved by employing *large* amplitudes and *low* frequencies. Explicitly, we attempted to observe wavy phenomena by choosing the frequency range below 20 Hz. For such low frequencies significant velocities are achieved by increasing the vibrational amplitudes A up to 3 cm. In parallel, a theoretical model of vibrated layers is developed, which is aimed at a calculation of the average values of the layer properties, including kinetic energy of granular random motion, particle number concentration, and the speeds of sound and of shock waves propagating through the vibrated layers. Thus, dimensionless parameters governing the appearance of wavy phenomena are introduced and expressed via the layer dimensions, granular properties and the vibrational parameters.

Generally, motion of bulk materials is affected by particle–air interactions. This effect is especially important for fine particles and powders (Thomas *et al.* 1987, 1989; Fauve *et al.* 1989). Aiming at an investigation of pure vibrational effects, stipulating particle–particle and wall–particle interactions, in the present study heavy particles were used (5 mm glass spheres), the motion of which was not significantly affected by the gaseous phase.

2. Experimental setup and three vibrational regimes

The experimental setup (figure 1) consisted of a 'two-dimensional' rectangular vessel, electrical motor with rotational velocity controller, eccentric transformer from rotational to translational motion, devices controlling the frequency and the phase of the vessel's vibrations, and a video-visualization system. The transparent walls of the vessel were made from two 260×260 mm Perspex plates fixed in an aluminium frame. The vessel was packed with $\sigma = 5$ mm diameter glass spheres. The restitution coefficient of the glass spheres was measured and found to be $e = 0.88$.

The gap between the plates was 7 mm, which slightly exceeded the particle's diameter. Thus, the motion of all particles could be visualized and recorded. The vessel was vertically vibrated by an electromechanical system which allowed discrete changes of the vibrational amplitude and continuous frequency changes.

Control of the rotational velocity (vibrational frequency) was done by means of an

electro-optical tachometer. The distribution of particles within the vessel was recorded by a video-camera with the exposure times, $t_e = 1/4000$ s or $1/250$ s. Recordings were made at several constant frequencies and amplitudes, and photographs of the vibrated layer were taken from the video film.

The vibrational regimes studied are characterized by the amplitudes 0.5, 1, 2, 3 cm and the frequency continuously varying from 0 to 20 Hz with accuracy better than 0.5 Hz. The temporal dependence of the vibration amplitude of the vessel was close to sinusoidal. The experiments were carried out for the bed thicknesses h_m of 5, 10, 15, 20 particle monolayers. In some of the experiments the vessel was divided by vertical partitions in two different proportions: $\frac{1}{4}:\frac{1}{2}:\frac{1}{4}$ or $\frac{1}{4}:\frac{3}{4}$.

Visualization of mixing processes within the vibrated vessel was achieved by introducing in the vessel several glass spheres (of the same diameter) painted black.

The experiments were performed by gradually increasing the vibrational frequency f from zero, with the amplitude kept constant. It was found that for sufficiently small f all the particles oscillated while closely contacting each other, which resembled the behaviour of a solid body. With increasing frequency this 'solid-like' vibrational state changed and the layer behaviour was characterized by transverse surface waves propagating across the layer width, similar to gravitational waves in liquid layers. Accordingly, this vibrational state was termed a 'liquid-like' or 'transverse-wave' state.

These transverse waves disappeared with further increasing of f. In this regime vigorous collisional motion of particles was observed, accompanied by compression and expansion waves propagating across the layers. Since these phenomena resembled those occurring in molecular gases, the corresponding vibrational state was termed a 'gas-like' state.

Detailed descriptions of the processes observed in each of the three vibrational states are given in the following section.

3. Experimental observations

3.1. *Solid-like vibrational state*

It was found that for thick layers ($h_m/\sigma \geqslant 5$ particle monolayers, where h_m is the layer thickness and σ the sphere diameter) at small vibrational frequencies ($\Gamma < 1$) the layers do not detach from the vessel's bottom (non-detaching regime). For $\Gamma \geqslant 0.5$ the free (upper) surface of the vibrated layers was smooth (figure 2*b*). One can see that the particles are organized in a structure possessing both short-range and long-range order similar to the solid crystal lattice structure. Accordingly we termed the latter particle state as 'solid state'.

Further increasing frequency f (when accelerations Γ exceeded 1) leads to the detachment of the layer from the bottom. This generally accords with predictions of theoretical models which view the vibrated layer as a solid plastic body (Chlenov & Mikhailov 1972; Gray & Rhodes 1972). Both periodic and aperiodic vibrational regimes were observed. In the periodic regimes, characterized by period τ, one, two and multiple modes were identified, where the vessel met the layer every one, two, etc. vibrational periods, i.e. $\tau = nT$ $(n = 1, 2 \ldots)$, with $T = 1/f$. In general, the modes' multiplicity increased with increasing dimensional acceleration Γ.

In the detaching regime the period τ may be divided into two parts: (i) t_f, when the layer is in the free flight, and (ii) $t_c = \tau - t_f$ when it moves together with the vessel. The ratio t_c/t_f was found to decrease with increasing Γ.

The above observations are in a qualitative agreement with predictions of the layer

(*a*)

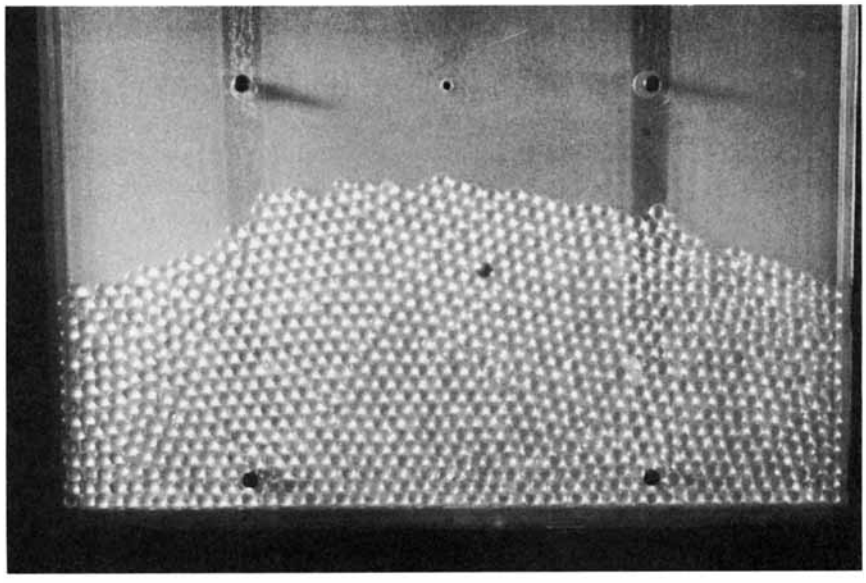

(*b*)

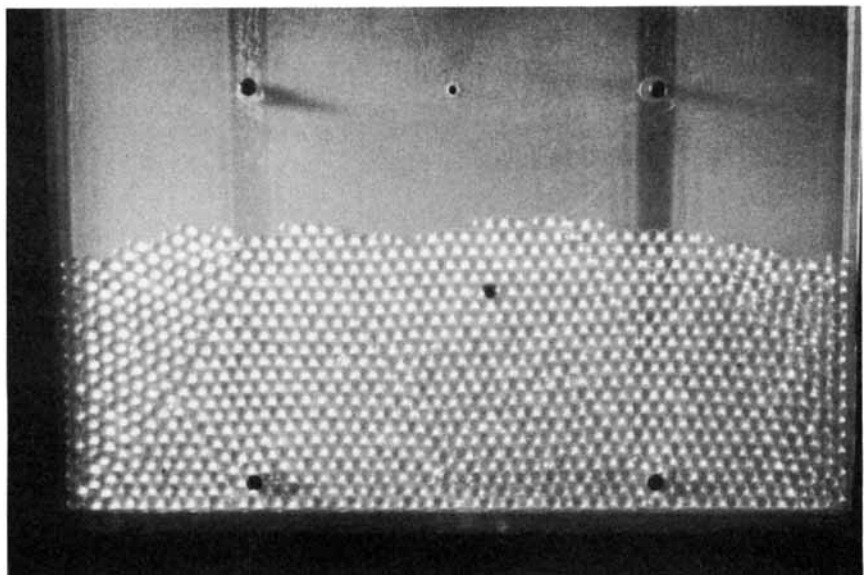

FIGURE 2. Photographs of the granular layer in the non-detaching vibrating regime: (*a*) before application of vibrations ($\Gamma = 0$); (*b*) in the process of vibrations ($A = 1$ cm, $f = 5$ Hz, glass beads of diameter, here and below, $\sigma = 5$ mm, $h_m = 15$ monolayers, $t_e = 1/4000$ s).

behaviour as a solid plastic body (Blekhman & Dzhanelidze 1964), as well as the experimental data of Gray & Rhodes (1972).

The 'detaching' and 'non-detaching' solid-state vibrational regimes are separated by the line $\Gamma = 1$, shown in figure 3, which depicts various vibrational states in the (A,f)-plane. When the vibrational frequency increased beyond the value $\Gamma = 1$ the uppermost particles jumped above the layer (see figure 4*a*). The ordered packing

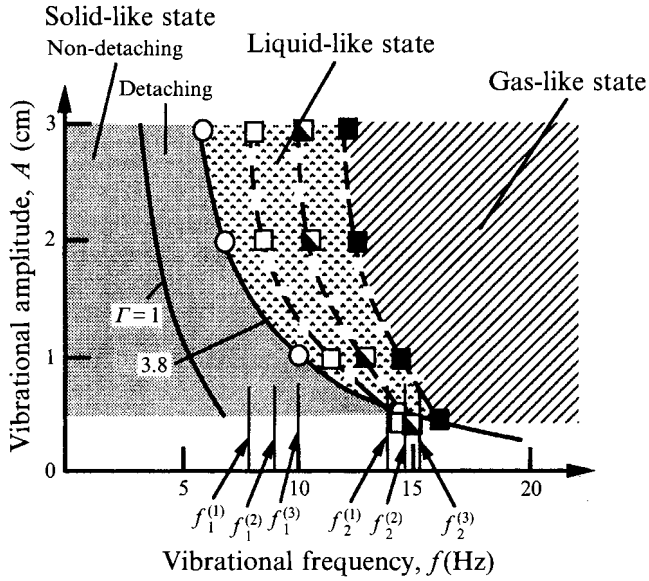

FIGURE 3. Diagram of the vibrational regimes of vibrofluidized granular layers. Solid lines: theoretical. Experimental data: ○, lower bound (beginning) of the transverse wave regime (all h_m). Upper bound (end) of the transverse wave regime: □, $h_m = 20$ monolayers; ◪, $h_m = 15$ monolayers; ■, $h_m = 10$ monolayers. $f_1^{(1)}, f_1^{(2)}, f_1^{(3)}$ are resonance frequencies (see (14)), calculated for $n = 1$ and for $h_m = 10$, 15 and 20 monolayers, respectively; $f_2^{(1)}, f_2^{(2)}, f_2^{(3)}$ are similar frequencies, calculated for $n = 2$.

arrangement is distorted and the total bed porosity increases. In fact, these jumps stem from the particle collisions (see §5 and table 2 below).

During the free flight period the layer porosity is larger than during the contact period (figure 4*a*, *b*). This behaviour of the vibrated bed is similar to the observations of Thomas *et al.* (1989) for powders at $\Gamma = 4$, $f = 25$ Hz, with the corresponding vibrational regime named 'coherent-expanded' state.

3.2. *Liquid-like (or transverse wave) state*

Increasing the vibrational frequency beyond the value corresponding to $\Gamma \sim 3.8 \pm 0.2$ leads to transverse bending of the layer due to transverse waves within it (see figures 5, 6). In this regime particle collisions occur more vigorously than in the detaching solid-state regime, which results in larger porosity in the upper and the lower parts of the vibrated layer (see figure 5). Both the transverse waves and particle collisions destroy the long-range interparticle order, although the short-range order is still sustained in some parts of the layer.

This wavy behaviour resembles the comparable process observed in liquid layers. Therefore the corresponding vibrational state may be termed a 'liquid-like state'. This state was found to prevail for thick layer (exceeding 5 monolayers) and only for vibrational amplitudes exceeding $A = 5$ mm. The domain corresponding to this state lies above the line $\Gamma = 3.8$ in the (A,f)-plane (see figure 3).

In the liquid-like (transverse wave) vibrational state the peripheral wave edge comes into contact with the vessel's bottom earlier (see figure 5*a*) and detaches from it earlier (see figure 5*b*). The volume of the layer increases with increasing frequency (see figure 6). The upper frequency boundary of the transverse wave state was found to depend upon the layer thickness h_m (see figure 3).

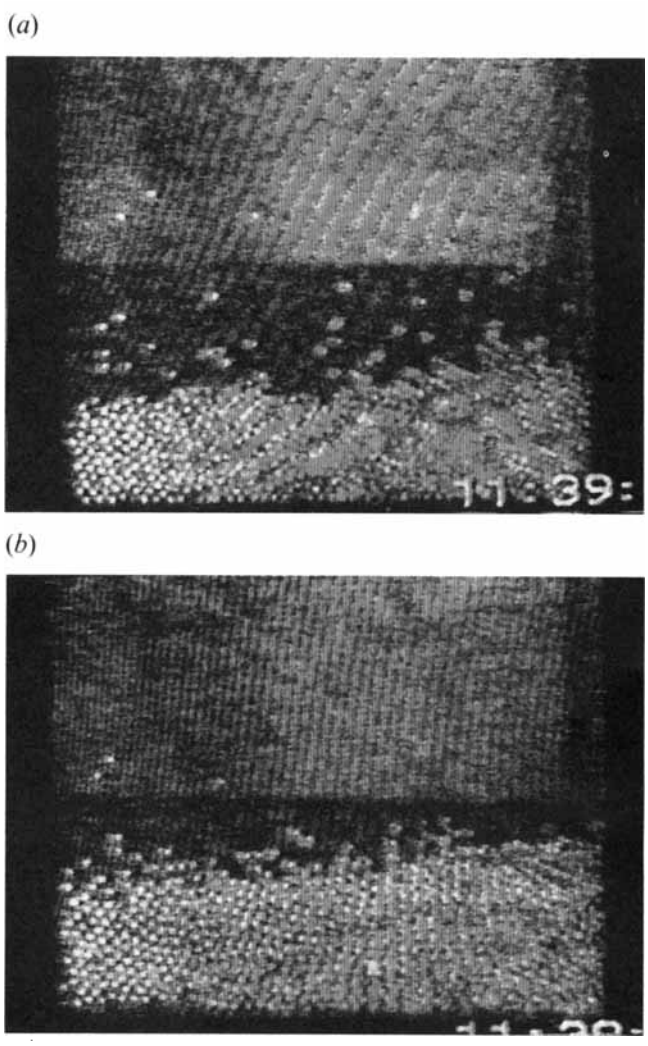

FIGURE 4. Photographs of compression and expansion of the granular layer (weakly detaching regime, $A = 3$ cm, $f = 5$ Hz, $h_m = 15$ monolayers, $t_e = 1/4000$ s). (*a*) Expansion of granular bed in the free flight; vessel moves down. (*b*) Compression of bed during the period of upward motion together with the vessel.

3.3. *Gas-like (compression–expansion wave) state*

With f increasing beyond the upper frequency boundary of the liquid-like state, no more transverse waves were observed. In this regime the collisional character of the particle motion is most obvious (see figures 7, 8). The intensity of collisions is larger than in the liquid-like regime, which results in a more uniform porosity distribution through the layer height (see figure 8). The porosity of the lower part of the layer is larger than in the middle. This is in contrast with the transverse wave state, where the maximum of the particle number density is in the lower part of the layer.

An increase of the layer uniformity with increasing frequency occurs because of the wavy character of the momentum transfer in the vertical direction within the layer. The photograph in figure 7, taken with the larger exposure time, shows the dispersion of particle velocities in the lower part of the layer, which is caused by the compression of the granular gas by the vessel's bottom moving upwards (compression wave).

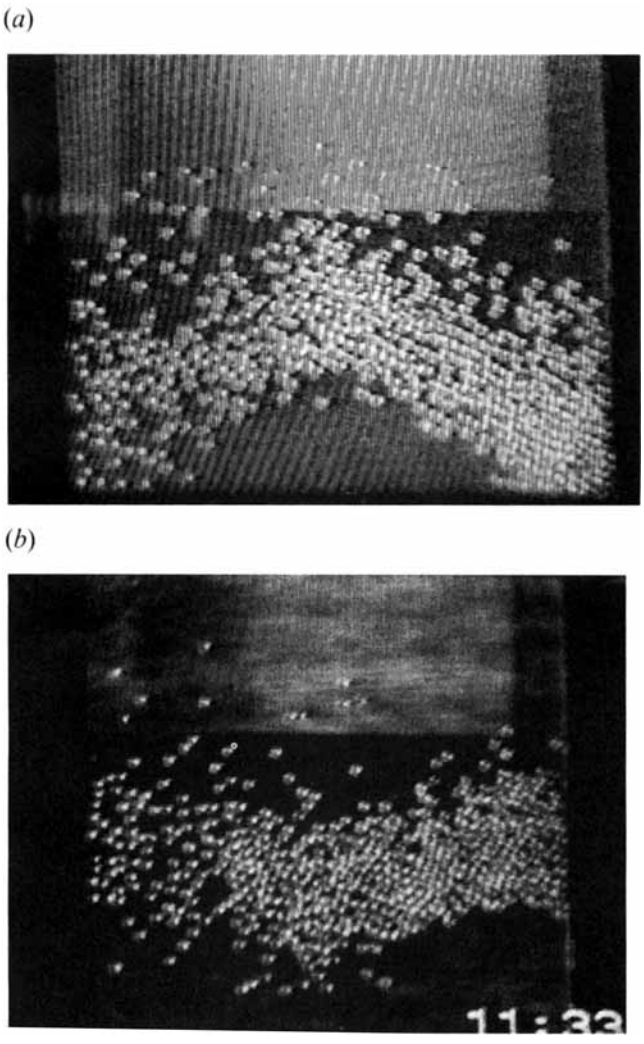

FIGURE 5. Photographs of the granular bed in the transverse wave state ($A = 3$ cm, $f = 10$ Hz, $h_m =$ 10 monolayers, $t_e = 1/4000$ s). (*a*) Meeting of vessel with the lower part of the bending layer; vessel moves up. (*b*) Vessel moves down after detaching from the granular layer. Notice that the layer curvature changes sign.

In figure 7 particle images in the lower part of the layer possess ellipsoidal shape. The length and orientation an ellipse's longer axis shows the magnitudes and directions of the particle velocity. However, particle images in the upper part of the layer appear as circles, which means that in this region the particles are stagnant.

The thickness of the transition region between these ellipsoidal and circular shapes is of the order of several particle mean free paths. In molecular gases such a small transition region is pertinent to shock waves, rather than to compression waves where the transition region is relatively thick. Accordingly, the above waves will be termed shock waves. Additional arguments supporting this term are provided in §5 on the basis of estimates of the wave front propagation speed.

An expansion wave is shown in figure 8, where one can see that the particle concentration in the lower part of the layer is less than that in the middle. This expansion wave is formed during the detachment of the layer from the vessel's bottom

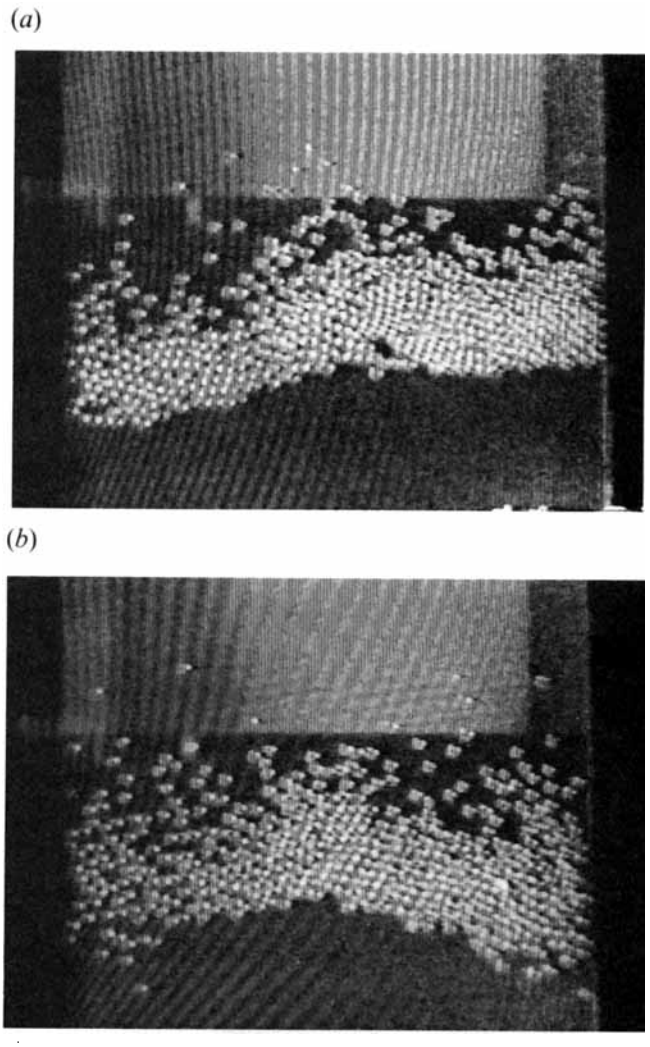

FIGURE 6. Influence of the vibration frequency f on layer porosity in the transverse wave (liquid-like) state. ($A = 3$ cm, $h_m = 10$ monolayers, $t_e = 1/4000$ s); (*a*) $f = 7$ Hz, (*b*) $f = 10$ Hz. The layer porosity increases with increasing frequency f.

and the free-flight stage, and may be explained by transformation of the energy of particles random motion into the kinetic energy of their averaged motion.

3.4. '*Phase transition*' *diagram*

The behaviour of granular layers observed for high-amplitude vibration regimes ($A \geqslant 5$ mm) with gradually increasing frequencies resemble the respective behaviour exhibited by solid bodies, (incompressible) liquids and gases. These concepts were used as a basis for classification of the vibrational states of granular layers. The frequency boundaries representing 'phase transitions' were obtained by observing the recorded material and identifying the respective frequencies of appearance and termination of the transverse wave phenomena. The results of the observations are graphically shown in figure 3 for various bed heights. Note that uncertainties in determination of the frequencies separating different vibrational states are comparable with the size of the symbols.

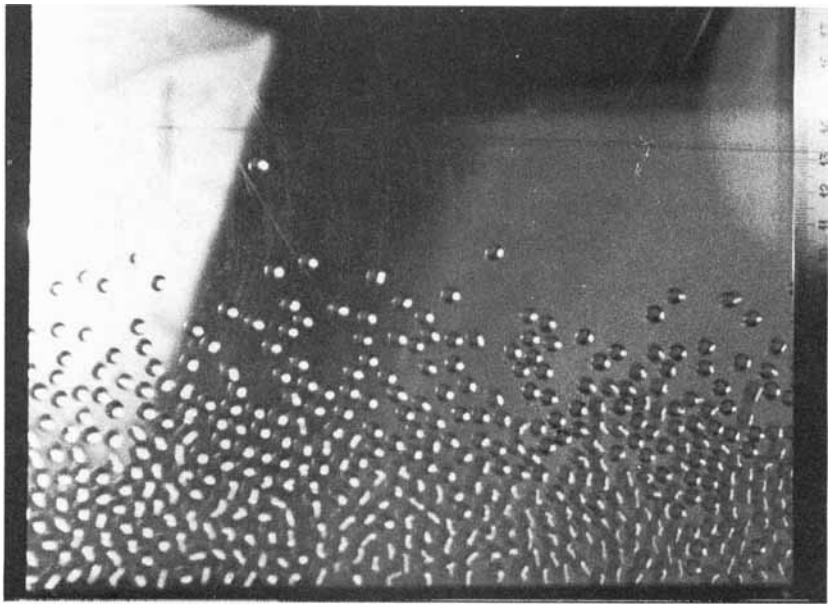

FIGURE 7. Compression (shock) wave within the vibrofluidized bed (vessel moves up, $A = 1$ cm, $f = 15$ Hz, $h_m = 10$ monolayers, $t_e = 1/250$ s). Ellipsoidal forms of the particle images in the bottom part the layer are caused by their motion with velocities up to 2 m s^{-1} in the direction of the long ellipses' axes.

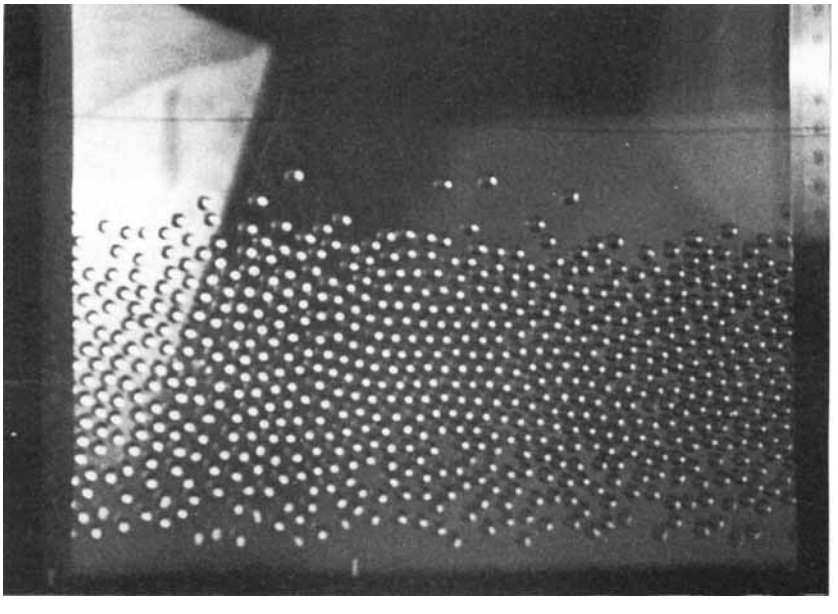

FIGURE 8. Expansion wave within vibrofluidized bed ($A = 1$ cm, $f = 10$ Hz, $h_m = 15$ monolayers, $t_e = 1/4000$ s). The porosity of the lower part of the granular layer is larger than that of the middle part.

The areas lying to the left and downward of the transverse wave domains correspond to the solid-state vibrational regime. The areas lying to the right and above transverse wave domains correspond to the granular gas state. The frequencies separating the liquid-like and the gas-like states were found to depend upon the layer height. One can

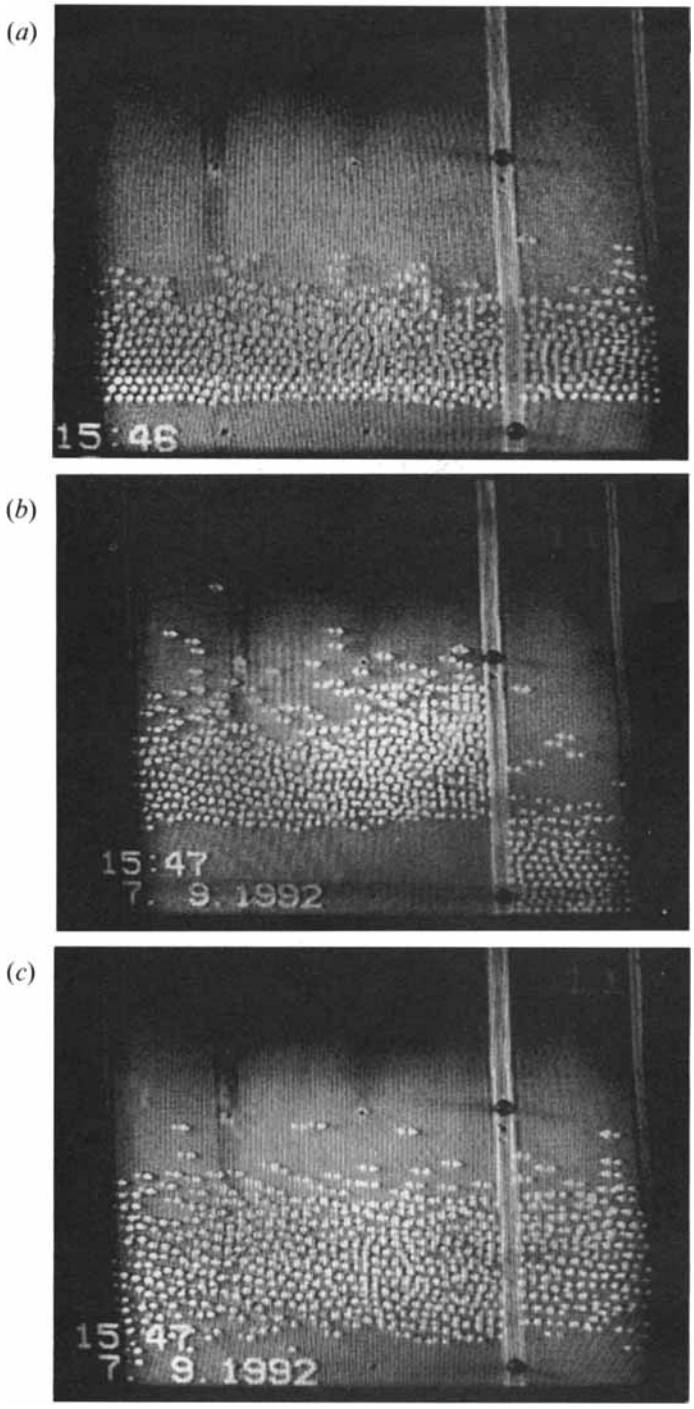

FIGURE 9. Synchronization and desynchronization in the vibrated layer ($A = 2$ cm, $h_m = 10$ monolayers, $t_e = 1/4000$ s): (*a*) synchronization regime ($f = 6$ Hz corresponding to the solid-like state); (*b*) desynchronization regime ($f = 8$ Hz corresponding to the liquid-like state); (*c*) synchronization regime ($f = 13$ Hz corresponding to the gas-like state). The length of the vessel is divided in the proportion 1:3.

see from the diagram that, for a fixed amplitude, decreasing the layer height leads to an increase of the frequency range in which the transverse wave regime exists. Alternatively, the frequency range of existence of the latter regime increases with increasing amplitude for a fixed layer height. For the heights $h_m/\sigma = 15$ and 20 particle monolayers and $A = 0.5$ cm the transverse wave regime was not observed.

3.5. *Other phenomena observed in vibrofluidized layers*

Several interesting phenomena had been found during observations of the behaviour of simultaneously vibrating granular beds: particle circulations, cavern formation and synchronization. The latter phenomenon was observed in experiments with vessel divided by vertical partitions in different proportions: $\frac{1}{4}:\frac{1}{2}:\frac{1}{4}$ or $\frac{1}{4}:\frac{3}{4}$. In the solid- and gas-like states layers of different widths were observed to simultaneously detach from and meet with the vessel's bottom, i.e. the moments of detachment and meeting were found to be independent of the layer width. This may be seen in figure 9(*a–c*), which shows partitioned layers composed from 10 monolayers in the three vibrational regimes. Synchronization is clearly observed in the solid and gas states (figure 9*a*, *c*), while it is absent in the liquid-like state (figure 9*b*).

Such a synchronization of the vibrational motion of different layers is pertinent to the motions of solid bodies (e.g. synchronization of two oscillating pendulum clocks attached to the same wall). This constitutes one more argument supporting the terminology chosen for describing the solid-like regime.

The velocities of individual particles were observed to significantly differ from the average layer velocity. This velocity dispersion is clearly seen in figure 7 for the gas state. To investigate this phenomenon in other vibrational regimes several particles were covered with a thin layer of black paint. Such a coating only affects particle surface properties and according to the results of Ahmad & Smalley (1973) does not lead to any significant segregation of black particles.

Experimental observations showed that the solid-like vibrational state is characterized by particle circulations, and thus differs from real solid-body behaviour. For a fixed amplitude A the circulation flux was found to reach a maximum at a certain frequency f_0, dependent upon the layer thickness. In particular, for $A = 0.5$ cm in the beds composed of 15 monolayers of transparent spheres and one layer of black spheres, circulative motion starts at the frequency where the bed begins to detach from the bottom and prevails up to $f = 15$ Hz. Two circulation loops are formed, in which the particles go down at the bed's centre and rise in the regions next to the vessel's walls. One such loop may be seen in figure 10.

In general three mixing mechanisms were observed in vibrating layers: circulations in the solid regime; transverse waves in the liquid regime and particle collisions in the gas-like state.

The circulation velocity was found to increase with increasing vibrational amplitude. Particle circulations were observed only in the solid-like state, and were not identified in the liquid-like state, where they are apparently destroyed by the transverse waves. For the gas state the mixing mechanism is particle random motion. In this state particle circulation is either absent or dominated by the more powerful mixing mechanism.

For amplitudes $A > 2$ cm large inhomogeneities were observed within the layers, in particular the formation of caverns (see figure 11). This phenomenon is well known in vibrofluidized powder technology (Chlenov & Mikhailov 1972), where it results from the 'pumping effect' stemming from gas–particle interactions. In the present study, performed with bigger particles, the caverns are formed as a result of wave propagation and are not related to gas–particle interactions.

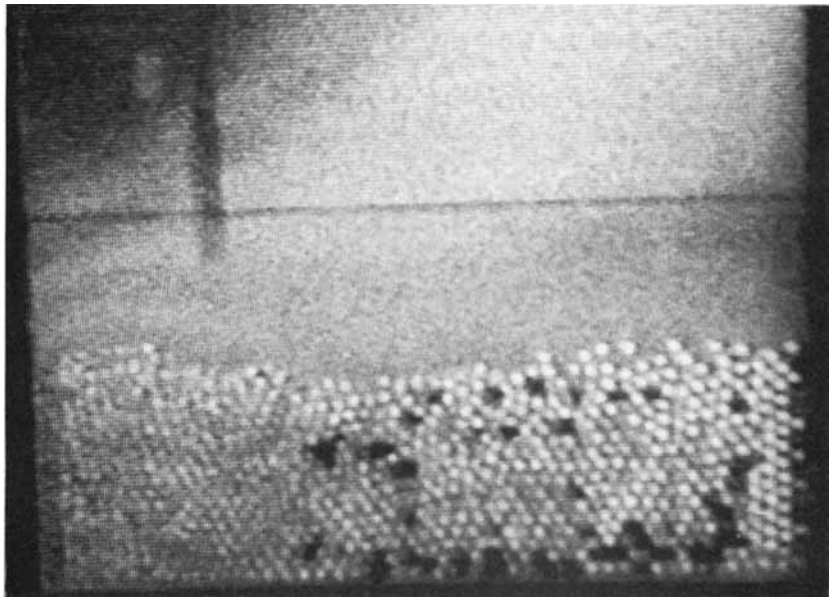

FIGURE 10. Circular motion of granules within the vibrated layer ($A = 0.5$ cm, $h_m = 20$ monolayers, $f = 10$ Hz, $t_e = 1/4000$ s). Visualization of the circulations is done by introducing in the layer black glass beads of the same diameter.

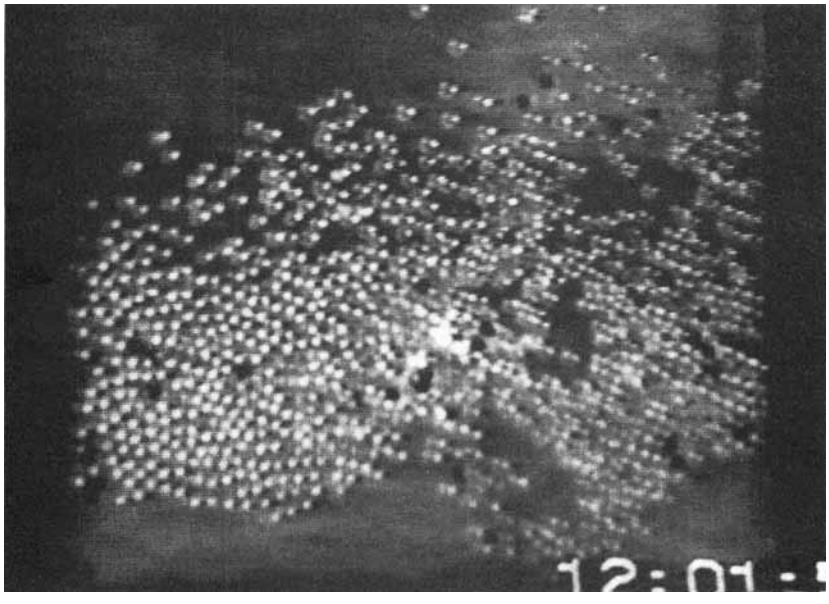

FIGURE 11. Formation of caverns within the vibrofluidized granular layer ($A = 3$ cm, $h_m = 20$ monolayers, $f = 7.5$ Hz, $t_e = 1/4000$ s).

4. Interpretation and modelling of the observations

4.1. *Solid-like regime*

The granular layer vibrated in the detaching solid-like regime may be approximately described by viewing it as a single solid block undergoing inelastic collisions with a wall (Chlenov & Mikhailov 1972). In the detaching regime of multiplicity n, one has

$$\tau_f + \tau_c = \tau = nT, \tag{1}$$

where τ_c and τ_f are the periods when the layer moves in contact with the wall and in free flight, respectively. This means that the layer comes in contact with the wall every n vibrational periods.

Assuming the vessel's motion $x_w(t)$ to be harmonic, one can write the following equations of motion:

$$x_l(t) = x_w(t) = A\sin(\omega t) = A\sin(2\pi t/T) \quad \text{during contact } (\ddot{x}_l(t) \geqslant -g), \tag{2}$$

$$\ddot{x}_l(t) = -g, \quad \text{in free flight,} \tag{3}$$

where x_l is the coordinate of the lowermost plane of the layer. At the moment of detaching, say t_d, both of the above equations are valid, i.e.

$$A\omega^2 \sin(\omega t_d) = g. \tag{4}$$

On the other hand, at the moment of meeting with the bottom, t_m,

$$A\sin(\omega t_m) = x_l(t_m). \tag{5}$$

In terms of t_m, t_d, one can write (see figure 12; note that $t'_m = t_m - \tau$)

$$t_m - t_d + \tau_c = nT = \tau. \tag{6}$$

The problem (2)–(5) may be solved to yield the values of $t_m, t_d, \tau_c = t_d - t'_m, \tau_f = t_m - t_d$ as functions of the acceleration parameter Γ. These results together with the non-dimensional layer velocity relative to the moving vessel at the moment of meeting are presented in table 1.

We will use the results of the single-body model for large values of Γ in order to compare its predictions with the layer motion observed in the gas-like state. In general, this motion is more complicated and differs from the single-body behaviour. In particular, the density of the layer differs from the maximal packing density, since the layer is expanded. However, several parameters of such expanded layers, were compared with the data shown in table 1; in particular, one can see that for $\Gamma \gg 1$

$$\bar{t}_d = t_d\omega \ll 1, \quad u_w(t_d) = \dot{x}_w(t_d) \approx A\omega. \tag{7a, b}$$

That is, the layer detaches from the wall when the wall's velocity is close to its maximal value. This conclusion accords with the experimental observations. More importantly, it was observed in the experiments that for large Γ the ratio

$$\tau_c/T \ll 1. \tag{8}$$

This observation, made in the gas-like vibrational state, is still in qualitative agreement with the solid-body model. Further, (6) together with the smallness of $\bar{t}_d = \omega t_d$ and $\omega\tau_c$ yields that at the meeting point $t_m \approx \tau$, or (see figure 12)

$$x_l(t_m) = x_w(t_m) \approx 0. \tag{9}$$

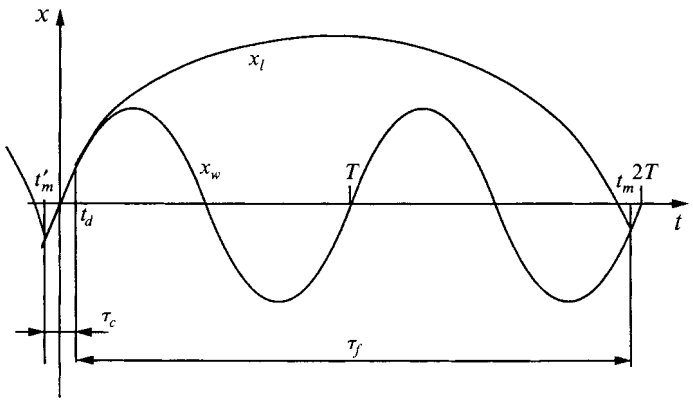

FIGURE 12. Kinematics of the single plastic body model of the solid-like regime.

$\tilde{t}_f/2$	Γ	$\tilde{t}_d$	$\tilde{t}_m$	$\tilde{t}_c$	$\tilde{t}_c/\tilde{t}_f$	$\tilde{u}_r = \tilde{u}_\tau - \tilde{u}_0$
$\pi/5$	1.05	1.26	2.52	5.0	3.98	0.08
$2\pi/5$	1.22	0.96	3.47	3.8	1.5	0.54
$3\pi/5$	1.58	0.68	4.47	2.5	0.66	1.39
$4\pi/5$	2.23	0.46	5.49	1.3	0.25	2.06
π	3.3	0.31	6.59	0	0	1.91
$6\pi/5$	4.33	0.23	7.77	5.0	0.67	0.85
$7\pi/5$	4.6	0.219	9.02	3.8	0.43	1.77
$8\pi/5$	4.69	0.215	10.27	2.5	0.25	0.5
$9\pi/5$	5.26	0.19	11.5	1.3	0.11	1.65
2π	6.36	0.16	12.72	0	0	1.98
$11\pi/5$	7.44	0.14	13.96	5.0	0.36	1.05
$12\pi/5$	7.79	0.129	15.21	3.8	0.25	0.07
$13\pi/5$	7.84	0.128	16.46	2.5	0.15	0.036
$14\pi/5$	8.37	0.12	17.71	1.3	0.07	1.53
3π	9.48	0.11	18.95	0	0	1.99

TABLE 1. Results of calculations for the solid plastic body model

Using (3) and (7*a*, *b*), one can write the following approximate expression for the layer velocity during the free flight:

$$u_l(t) = \dot{x}_l(t) \approx A\omega - g(t - t_d) \approx A\omega - gt. \tag{10}$$

Integration with the initial condition $x_l(t_m) \approx 0$ gives, during the free flight,

$$x_l(t) = A\omega t - gt^2/2. \tag{11}$$

Writing this equation at the meeting point, and using (9), one obtains

$$2A\omega \approx g\tau \quad \text{or} \quad \Gamma \approx n\pi. \tag{12a, b}$$

This result implies that

$$u_l(t_m) = \dot{x}_l(t_m) \approx = -A\omega. \tag{13}$$

The above result indicates that multi-period collisional regimes most clearly observed in this study prevail for vibrational frequencies and amplitudes related by (12*a*, *b*). In these regimes the relative wall-layer velocity at the meeting point is maximal and equal about $2A\omega$. The kinetic energy supplied to the layer by the wall, i.e. $2MA^2\omega^2$, is also maximal. This energy is partially converted into the granular random-motion kinetic energy, which leads to the layer expansion in the gas-like state.

The above conclusions and estimates will be used below in the model for shock wave propagation through the expanded layer prevailing in the gas-like collisional state.

4.2. *Transverse wave regime*

Bearing in mind the relatively narrow frequency range of existence of the transverse wave (liquid-like) regime, it may be inferred that this phenomenon has a resonance nature. Since chaotic particle motion in this regime is very weak, the characteristic frequency of the layer should be determined as the square root of the ratio of the gravitational acceleration g to some linear dimension. Since the transverse waves in granular layers are very similar to gravitational waves in liquids (Landau & Lifshitz 1987), one can use the formula for the characteristic frequencies

$$f_n = \left(\frac{gn}{4\pi L}\tanh\frac{n\pi h_m}{L}\right)^{1/2}, \quad n = 1, 2, \ldots \tag{14}$$

derived for the latter waves in a rectangular vessel of height h_m, length L and an arbitrary width. The integer value n describes the number of half-waves contained within the length L.

Calculations of f_1, f_2 using (14) for the ratio $h_m/L = 10/52,\ 15/52,\ 20/52$, corresponding to the experimental conditions, are presented in figure 3. One can see that the first two resonance frequencies fit into the range of existence of the transverse wave regime in granular materials. Formula (14) sufficiently accurately predicts the characteristic frequencies corresponding to the largest transverse waves amplitudes, as well as the wave shape (i.e. half-wave). Noting that (14) was derived for a continuous incompressible inviscid liquid (Landau & Lifshitz 1987), the above agreement appears to be surprisingly good.

The layer porosity (and consequently compressibility) was found to increase with increasing amplitude A. Moreover, for large vibration amplitudes ($A > 2$ cm) discontinuities, i.e. caverns, appear within the bed (see figure 11). This phenomenon was observed only for thick layers (more than 5 monolayers) and large amplitudes ($A >$ 2 cm). The discrepancies between the frequencies calculated by formula (14) and the measured data may be partially attributed to the appearance of these discontinuities.

The predictive power of (14) was investigated for other layer aspect ratios. For this purpose thin plates of Perspex were placed in the vessel, to divide its length in two parts (in proportion 1:3), and in three parts (in proportion 1:2:1). For a fixed layer height, h_m, decreasing layer length, L, leads to a monotonic diminution of the frequency range of existence of the transverse wave regime. However, this frequency range remains inside the corresponding range measured for the whole vessel, in accordance with formula (14).

Summarizing the above, one can state that (14) adequately correlates the central values of the frequency ranges for the liquid-like (transverse wave) states of the vibrofluidized granular layers. However, it cannot predict the lengths of the above intervals or their dependence on the vibration amplitude. In addition, (14) obtained for inviscid incompressible liquids can not predict amplitudes of the transverse waves. These amplitudes are governed by the liquid's viscosity (Landau & Lifshitz 1987), the value of which for vibrofluidized granular layers may be determined from kinetic theory (Jenkins & Savage 1983).

Fauve *et al.* (1989) observed layers of powders which bent in a spatially periodic manner when vibrated with frequencies of 20 Hz. They interpreted this behaviour as a standing wave, like in ordinary liquids. However, calculations by (14) show that the

resonance oscillation frequency for layers with the parameters reported in this work are much lower than 20 Hz. It is, however, possible, that this discrepancy can be attributed to the influence of gas-layer interactions. The latter can possibly also explain the bending of the layers of powders noted by Thomas *et al.* (1987). In their study the curvature of the layer did not change (with the central part of the layer being always higher than the peripheral parts). Therefore, this motion is clearly not of wavy origin, unlike the present study where the layer curvature changed periodically.

In contrast with above studies we used relatively large heavy particles, for which particle–air interactions are negligible. Therefore the transverse waves that we observed in vibrated granular beds are a new phenomenon, arising due to a gravitationally induced instabilities.

4.3. *Collisional gas-like state*

4.3.1. *General*

In this subsection observations made in the collisional regime are interpreted by employing the hydrodynamic equations describing the transport and evolution of the macroscopic granular properties, averaged over a representative volume (Jenkins & Savage 1983). Such equations are usually derived by application of the kinetic theory developed for molecular gases (Chapman & Cowling 1970). Clearly the kinetic theory of the collisional granular motion is unable to yield as accurate a description of the rapid granular flows as it does for flows of molecular gases. It stems *inter alia* from a relatively small number of particles within the representative volume (over which the averaging is performed). However, the experiments of Drake (1990) with rapid shear granular flows, showed that an averaging area with the height of 2 particle diameters and length of 14 diameters provides a sufficiently accurate hydrodynamic description (for more details see Drake 1990).

Wave propagation processes in vibrofluidized layers are characterized by an additional degree of complexity compared to steady granular flows, since these processes are inherently unsteady and non-homogeneous. The goal of the treatment given below is to use the hydrodynamic equations for estimation of the average properties of vibrated granular layers.

4.3.2. *The Euler hydrodynamic equations of collisional motion*

Consider the particles as identical spheres of radius σ in collisional motion. We will consider these collisions as instantaneous, as is done for molecular gases. Viewing the layer as a granular gas (Jenkins & Savage 1983), one can characterize its collisional state by the hydrodynamic properties: granular gas mass concentration ρ (related to the number concentration n via $\rho = mn$), velocity u, pressure P, and energy of random granular motion per particle E.

We will restrict considerations to regimes for which the particle concentration ρ is close to the maximum packing density, ρ_m (see figure 2*a*), i.e.

$$\Delta \equiv 1 - \rho/\rho_m \ll 1. \tag{15}$$

Neglecting the inelasticity of the granules one can write the equation of state of the granular gas in the form (Alder & Hoover 1968)

$$P = \frac{2\rho_m E}{m\Delta}, \tag{16}$$

which is valid for simple gases consisting of elastic smooth particles.

It may be shown that the error introduced in (16) by neglecting particle inelasticity may be represented by the factor $(1+e)/2$, with $0 < e < 1$ being the particle's restitution coefficient, which in the present case of glass beads is 0.94. The non-conservative nature of the particle collisions is taken into account in the equation governing the evolution of particle's kinetic energy (see (17*c*)).

A one-dimensional version of the Euler-like equations of an inelastic smooth granular gas may be written in the following form (Campbell 1990; Goldshtein & Shapiro 1995):

$$\frac{\partial \rho}{\partial t}+\frac{\partial}{\partial x}(\rho u)=0, \quad \frac{\partial}{\partial t}(\rho u)+\frac{\partial}{\partial x}(\rho u^2+P)=-\rho g, \tag{17a, b}$$

$$\frac{\partial}{\partial t}(nE+\tfrac{1}{2}\rho u^2)+\frac{\partial}{\partial x}[nu(E+\tfrac{1}{2}mu^2)+uP]=I(\rho, E), \tag{17c}$$

where $I(\rho, E)$, given by (Jenkins & Savage 1983; Goldshtein & Shapiro 1995)

$$I=-\frac{C(e)}{\sigma\Delta}\left(\frac{E}{m}\right)^{3/2}=-\frac{2}{\sigma\Delta}\left(\frac{6}{\pi}\right)^{1/2}(1-e^2)\left(\frac{E}{m}\right)^{3/2}, \tag{18}$$

is the energy sink term associated with the non-conservative nature of the particle collisions. In the above $C(e)=2(1-e^2)(6/\pi)^{1/2}$ is the coefficient dependent on the particle inelasticity, derived for three-dimensional granular systems. Although the distance between the walls of the vessel employed in the experiments only slightly (by 2 mm) exceeded one particle diameter, the three-dimensional granular gas model was used for the following reasons. The energy of chaotic particle motion is distributed between their available degrees of freedom. The availability of any degree of freedom is characterized by the particle's ability to move without collisions. Photographs presented in figures 4, 7 and 8 clearly show that the distances between the particles in the plane of the photograph (the mean free path) are of the order of several millimetres. Therefore, the gap between the vertical vessel's walls was of the same order of magnitude as the mean free path in each direction, which justified using three-dimensional model in the calculations.

Hydrodynamic equations of rapid flows of granular materials employed in previous studies (see e.g. Jenkins & Savage 1983) contain terms accounting for viscosity and heat conductivity. These effects are important in modelling rapid shear flows of granular media (Campbell 1990). However, similarly to the comparable processes in molecular gases, viscous phenomena are less important when modelling expansion and shock waves (see, for example, Moody 1990) and studies cited therein). Therefore, we neglect viscous interactions in (17*a–c*), thereby restricting our consideration to the Euler-like hydrodynamic model for describing wave propagation processes.

Equations (15)–(18) are subject to boundary conditions, which may be formulated as follows: when the wall moves upwards into the granular gas its velocity is equal to the wall's velocity

$$u=u_w(t) \quad \text{at the lower boundary if } P \geqslant 0. \tag{19a}$$

This equation is also valid when the wall withdraws from the gas until the moment of detaching $t=t_d$, which is described by the condition

$$P=0 \quad \text{at the lower boundary.} \tag{19b}$$

During the free-flight period the granular pressure at the top and the bottom edges vanishes. Accordingly, in this period (19*b*) is also employed at the upper free surface.

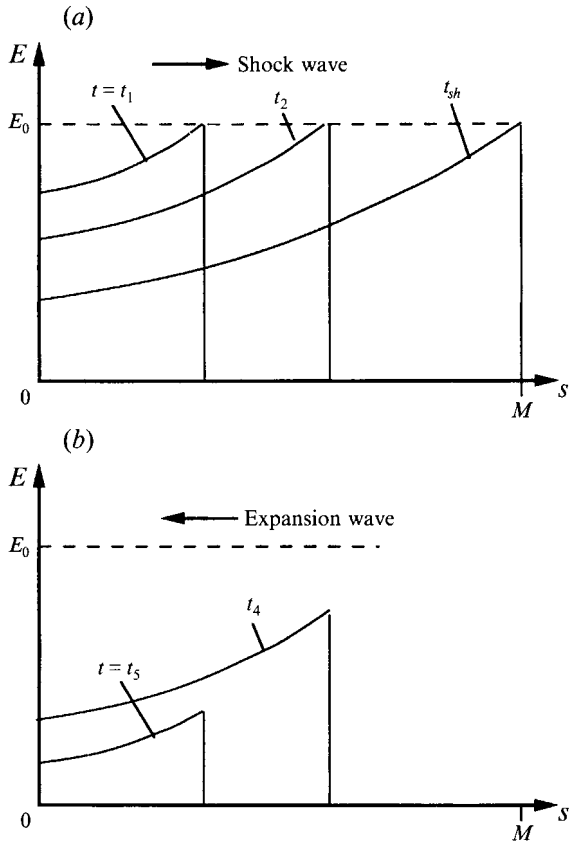

FIGURE 13. Distribution of kinetic energy of granular random motion across the vibrofluidized layer: (*a*) during shock wave propagation; (*b* during expansion wave propagation.

The process occurring within vibrated granular layers may be described by the following qualitative considerations. Consider collisional motion of the granular layer with a certain period $\tau = nT$. A short time after the layer comes in contact with the moving wall, the particle hydrodynamic velocity, u, near the wall becomes close to the wall's speed, whereas far from the wall the particles continue to move as in the free-flight stage (cf. figure 7). This velocity discontinuity (shock wave) propagates from the lowermost to the uppermost part of the granular layer with a speed D, creating particles' chaotic motion behind the front. This chaotic granular motion creates granular pressure P (and, hence, random motion energy E) within the disturbed region (see figure 13*a*). At the moment $t = t_{sh}$, when the shock wave reaches the layer top (where $P = 0$) an expansion wave is formed, which propagates from the uppermost to the lowermost part of the layer with the speed of sound a within the granular gas (Savage 1988).

When the expansion wave arrives at any plane s of the layer, part of the kinetic energy E_0 which it received from the vessel will dissipate due to inelastic particle collisions. The remaining part ($E(s)$) will be transformed by the expansion wave into the energy $m\Delta u_m^2/2$ of average particle motion, with Δu_m being the velocity relative to the motion of the layer's centre of mass. Owing to this energy transformation the particles involved in the expansion process will accelerate upwards. The expansion wave propagating downwards will successively pass 'cooler' granules, since there the

dissipation process, which began after the passage of the shock wave, occurred longer. Accordingly, for lower parts of the layer less kinetic energy E will be converted into average motion. Therefore, the upper parts of the layer will accelerate upwards faster (with larger Δu_m) than the lower ones. The hydrodynamic velocity gradient thus formed within the layer cause its expansion during free flight.

For analyses of the expansion wave propagation an expression for the speed of sound a is needed. For smooth elastic spheres this quantity is given by (Savage 1988; Goldshtein & Shapiro 1995)

$$a = \left\{\frac{E}{m}\left[\frac{\mathrm{d}}{\mathrm{d}n}\left(\frac{P}{E}\right)+\left(\frac{P}{nE}\right)^2\right]\right\}^{1/2}. \tag{20}$$

The above expression together with the equation of state (16) gives

$$a = \frac{1}{\Delta}\left(\frac{6E}{m}\right)^{1/2}. \tag{21}$$

In this formula the kinetic energy losses due to particle inelastic collisions will be implicitly accounted for in the expression for the energy E.

Complete formulation of the wave propagation problem should include conditions for changes of the hydrodynamic properties across the shock front (Goldshtein & Shapiro 1995). For equations (17*a–c*) with the dissipation term I given by (18) these conditions coincide with the Rankine–Hugoniot conditions (Courant & Friedrichs 1948), used for molecular gases:

$$[\![\rho(D-u)]\!] = 0, \quad [\![\rho(D-u)^2+P]\!] = 0, \tag{22a, b}$$

$$\left[\!\left[n(D-u)\left\{E+\frac{P}{n}+\frac{m}{2}(D-u)^2\right\}\right]\!\right] = 0, \tag{22c}$$

where D is the kinematic speed of the shock front and $[\![\ldots]\!]$ denotes the jump of any hydrodynamic property across the shock front. The energy dissipation term does not contribute to the above jump condition, neither does any volumetric sink/source term.

4.3.3. *Asymptotic solution for weakly expanded layers*

We will provide an approximate solution of equations (17*a–c*) aimed at establishing basic scaling relationships between the mean (i.e. average over the thickness and the period τ) layer properties and the vibrational parameters. Rewrite system (17*a–c*) using (15) in the Lagrangian form (Courant & Friedrichs 1948)

$$\frac{1}{\rho_m}\frac{\partial \Delta}{\partial t} = \frac{\partial u}{\partial s}, \quad \frac{\partial u}{\partial t}+\frac{\partial P}{\partial s} = -g, \quad \frac{\partial}{\partial t}\left(\frac{E}{m}\right)+P\frac{\partial u}{\partial s} = I, \tag{23a–c}$$

where the layer mass variable s is calculated by integrating the particle mass density distribution from the lowermost possible piston position:

$$s(x,t) = \int_{-A}^{x} \rho(\xi,t)\,\mathrm{d}\xi. \tag{24}$$

Accordingly, the uppermost part of the layer corresponds to its total mass $s = M$, and the lowermost part to $s = 0$. Since all hydrodynamic layer properties are assumed to be time-periodic functions with period $\tau = nT$, the shock wave passes each point s within the layer once per period τ.

Using (24) one can rewrite the Rankine–Hugoniot relationships (22*a–c*) in the respective forms:

$$\left[\!\left[\frac{D_L}{\rho}+u\right]\!\right]=0, \quad \left[\!\left[\frac{P}{D_L}-u\right]\!\right]=0, \quad \left[\!\left[\frac{E}{m}+\frac{P}{\rho}+\frac{1}{2}\left(\frac{D_L}{\rho}\right)^2\right]\!\right]=0, \tag{25a–c}$$

where $D_L=(D-u)\rho$ is the mass speed of the shock front (function of s only). In addition, owing to the periodicity of the process the jump of any hydrodynamic property f (continuous in the interval $+0<\tilde{t}<\tau-0$) may be written in the form

$$[\![f]\!]=f|_{\tilde{t}=0}-f|_{\tilde{t}=\tau}, \tag{26}$$

where for any point s the local variable $\tilde{t}$ is chosen in such a way that $\tilde{t}=0$ at the moment when the shock wave passes through s, i.e. (see figure 12; note that $t_m-t'_m=\tau$)

$$\tilde{t}=\tilde{t}(t,s)=t-t'_m-\int_0^s \frac{\mathrm{d}s_1}{D_L(s_1)}. \tag{27}$$

At the moment $[\tilde{t}=0]$, when the shock front passes through a point s, the properties P, E, Δ at this location instantaneously increase. After that they decrease as a result of dissipation of the granular kinetic energy and its partial conversion into the energy of the average layer motion. Consequently, well before the moment $t=t_m-\tau$ of its next meeting with the wall the granular pressure, P_τ, and the energy, E_τ, associated with the random granular motion diminish to zero:

$$E_\tau=0, \quad P_\tau=0, \quad 0<s<M. \tag{28}$$

However, as will be shown below, during the free-flight period, $\Delta\neq 0$, since the layer expands due to the velocity gradient in it.

Conditions (28) imply that the situation considered here corresponds to the strong shock wave approximation (Courant & Friedrichs 1948). Using (7*b*), (13), (15) and (16) one can rewrite conditions (25*a–c*) in the respective forms

$$\Delta_0=\Delta_\tau/2, \quad P_0=D_L^2\Delta_\tau/(2\rho_m), \quad u_0=D_L\Delta_\tau/(4\rho_m). \tag{29a–c}$$

We will seek solutions for (23*a–c*) subject to the conditions (29) and (19) assuming that the hydrodynamic quantities weakly depend upon the coordinate s. This allows expansions

$$u(s,\tilde{t})=u^{(0)}(\tilde{t})+u^{(1)}(s,\tilde{t})+\ldots, \quad \Delta(s,\tilde{t})=\Delta^{(1)}(\tilde{t})+\Delta^{(2)}(s,\tilde{t})+\ldots, \tag{30a, b}$$

$$P(s,t)=P^{(-1)}(\tilde{t})+P^{(0)}(s,\tilde{t})+\ldots, \quad D_L(s)=D_L^{(-1)}+D_L^{(0)}(s)+\ldots, \tag{30c, d}$$

$$a(s)=a^{(-1)}+a^{(0)}(s)+\ldots, \tag{30e}$$

where generically

$$\phi^{(k)}=O(\Delta_0)^k, \quad k=-1,0,1,\ldots \tag{30f}$$

with ϕ being any of the expansion coefficients appearing in (30). The zero-order velocity $u^{(0)}(\tilde{t})$ is given by solution obtained for the solid plastic body model (cf. (2), (3)):

$$u^{(0)}(\tilde{t})=\begin{cases} A\omega\cos\omega(\tilde{t}+t'_m) & \text{for } 0\leqslant\tilde{t}\leqslant\tau_c, \quad (31a)\\ A\omega\cos\omega t_d-g(\tilde{t}-\tau_c) & \text{for } \tau_c\leqslant\tilde{t}\leqslant\tau, \quad (31b)\end{cases}$$

which is shifted by the time (see (27))

$$\int_0^s \frac{\mathrm{d}s_1}{D_L(s_1)}$$

due to the finite speed of shock propagation. This velocity together with the coefficients $\Delta^{(1)}$, $P^{(-1)}$, $D_L^{(-1)}$, $a^{(-1)}$ represent the leading-order solutions for a slightly expanded layer, which on average performs solid plastic body motion (31*a*, *b*). The scaling relationships for the expansion coefficients assumed in (30*a–d*) will be substantiated in the course of the solution and verified in the next section on the basis of the experimental data.

Introducing expansions (30*a–d*) in the system (23*a–c*) and using (30*f*) to separate terms of equal powers of Δ_0, one obtains the following system of equations:

$$\frac{\Delta^{(1)}}{\rho_m}\frac{\mathrm{d}P^{(-1)}}{\mathrm{d}\tilde{t}}+3\frac{P^{(-1)}}{\rho_m}\frac{\mathrm{d}\Delta^{(1)}}{\mathrm{d}\tilde{t}}=-\frac{C(e)}{\sqrt{2}\,\sigma}(\Delta^{(1)})^{1/2}\left(\frac{P^{(-1)}}{\rho_m}\right)^{3/2}, \tag{32a}$$

$$\frac{\partial u^{(1)}}{\partial s}=\frac{\mathrm{d}}{\mathrm{d}\tilde{t}}\left[\frac{\Delta^{(1)}}{\rho_m}+\frac{u^{(0)}}{D_L^{(-1)}}\right],\quad \frac{\mathrm{d}}{\mathrm{d}\tilde{t}}\left[u^{(0)}-\frac{P^{(-1)}}{D_L^{(-1)}}\right]=-\frac{\partial P^{(0)}}{\partial s}-g. \tag{32b, c}$$

Equation (32*a*) may be used to express $P^{(-1)}$, via the as yet unknown function $\Delta^{(1)}(\tilde{t})$:

$$P^{(-1)}(\tilde{t})=P_0\left[\frac{\Delta_0}{\Delta^{(1)}(\tilde{t})}\right]^3\left\{1+\frac{C(e)}{\sqrt{2}\,\sigma}\left(\frac{P_0}{\rho_m\Delta_0}\right)^{1/2}\int_0^{\tilde{t}}\left[\frac{\Delta_0}{\Delta^{(1)}(\xi)}\right]^2\mathrm{d}\xi\right\}^{-2}, \tag{33}$$

subject to the initial conditions

$$P^{(-1)}(0)=P_0,\quad \Delta^{(1)}(0)=\Delta_0. \tag{34}$$

The system (32*a–c*) contains four unknown functions. Therefore an additional condition is needed. To provide an additional condition integrate (32*b*) over the period and use (15), (29*a*, *c*) to obtain

$$\int_0^{\tau}\frac{\partial u^{(1)}}{\partial s}\mathrm{d}\tilde{t}=\left[\frac{\Delta^{(1)}}{\rho_m}+\frac{u^{(0)}}{D_L^{(-1)}}\right]_0^{\tau}=0,$$

i.e. the velocity gradient averaged over the period is zero. This allows it to be assumed that $\partial u^{(1)}/\partial s=0$ which allows (32*b*) to be reduced to the form

$$\frac{1}{\rho_m}\frac{\mathrm{d}\Delta^{(1)}}{\mathrm{d}\tilde{t}}\approx\frac{1}{D_L^{(-1)}}\frac{\mathrm{d}u^{(0)}}{\mathrm{d}\tilde{t}}. \tag{35a}$$

Now the system (32*a*, *c*), (35) may be integrated to obtain

$$\Delta^{(1)}(\tilde{t})-\Delta_0\approx-\frac{\rho_m}{D_L^{(-1)}}[u^{(0)}(\tilde{t})-u_0], \tag{35b}$$

where the following boundary conditions were satisfied:

$$\tilde{t}=0:\quad u^{(0)}=u_0=A\omega\cos\omega t_m\approx A\omega,\quad \Delta^{(1)}(0)=\Delta_0. \tag{35c}$$

We now use (4), (31), (12*a*), (35*c*), jump conditions (29*a*, *c*) and condition $\omega\tau_c\ll 1$ (see (8)) to estimate the left-hand side of (35*b*) during the contact period $0<\tilde{t}<\tau_c$:

$$\begin{aligned}\Delta^{(1)}(\tilde{t})-\Delta_0\leqslant\Delta^{(1)}(\tau_c)-\Delta_0&=-\frac{\rho_m}{D_L^{(-1)}}[u^{(0)}(\tau_c)-u_0]\\&\approx\tau_c\frac{\rho_m}{D_L^{(1)}}A\omega^2\sin(\omega t_d)\\&=\frac{\tau g\rho_m}{D_L^{(-1)}}\left(\frac{\tau_c}{\tau}\right)\ll\frac{2\rho_m u_0}{D_L^{(-1)}}=\Delta_0.\end{aligned} \tag{36}$$

One can, therefore, see from (35*a*), (36) that $\Delta^{(1)}(\tilde{t})$ changes insignificantly during the contact period and in (33) set $\Delta^{(1)}(\tilde{t}) \approx \Delta_0$ to obtain

$$P^{(-1)}(\tilde{t}) = P_0\left[1+\tilde{t}\frac{C(e)}{\sqrt{2}\,\sigma}\left(\frac{P_0}{\rho_m \Delta_0}\right)^{1/2}\right]^{-2}. \tag{37}$$

This result accords with the solutions of Raskin (1975) and Haff (1983) describing the decay of granular pressure in the absence of gradients of hydrodynamic functions.

The above formula predicts the diminution of the pressure at each point within the layer until the moment of arrival of the expansion wave, which propagates downwards from the uppermost plane. This process starts at the time moment $t = \tau_{sh}$, when the shock wave reaches the uppermost plane of the layer. We will use this result together with the jump conditions (29*a–c*) to estimate the layer properties P_0, E_0, $D_L^{(-1)}$.

4.3.4. *Estimation of the layer vibrational properties*

Substituting u_0 and u_τ respectively from (35*b*) and (13) into jump conditions (29*c*) and combining the result with (29*a*, *b*), one obtains

$$D_L^{(-1)} \approx D_L = \frac{2A\omega}{\Delta_0}\rho_m, \quad P_0 = \frac{4A^2\omega^2}{\Delta_0}\rho_m. \tag{38a, b}$$

Using the above, one can express the time τ_{sh} of the shock wave propagation across the layer in the form

$$\tau_{sh} \approx \frac{M}{D_L} = \frac{h_m \Delta_0}{2A\omega} = \frac{h_m \Delta_0}{g\tau}. \tag{39}$$

After the shock wave reaches the top of the layer, where the granular pressure is zero (see (19*b*) and the immediately following paragraph), an expansion wave is formed, which propagates downwards with velocity $a \approx a^{(-1)}$. The effect of this wave is to convert the kinetic energy of random granular motion into the kinetic energy of the average motion. As in molecular gases (Courant & Friedrichs 1948), such a conversion takes place without discontinuities in hydrodynamic properties during a certain finite time. In the model we will, however, for simplicity assume that the random-motion kinetic energy E prevailing at a point s_{exp} at the moment when the expansion wave passes it, is *instantaneously and fully* converted into the kinetic energy of the average granular motion. In the coordinate system fixed with the moving piston this assumption is written in the form

$$E(s_{exp}) = m[\Delta u_m(s_{exp})]^2/2, \tag{40a}$$

where Δu_m is the velocity gain immediately after the conversion. Therefore, behind the expansion wave one has $E = 0$ (see figure 13*b*).

As the expansion wave propagates downwards, the upper layers will move under the action of gravity, the effect of which is to diminish the initial maximal velocity gain Δu_m given by (40*a*) according to the expression

$$\Delta u(s_{exp}, t) = \Delta u_m(s_{exp}) - g[t - t_{exp}(s_{exp})], \quad t_{exp}(s_{exp}) < t < t_{exp}(0), \tag{40b}$$

where $t_{exp}(s_{exp})$ is the time taken for the expansion wave to pass from the uppermost plane $s = M$ to the current plane $s = s_{exp}$:

$$t_{exp}(s_{exp}) = -\int_M^{s} \frac{\mathrm{d}\xi}{\rho_m\, a(\xi)}. \tag{40c}$$

Accordingly, (40*b*) accounts for the gravitational loss of the velocity gain occurring during the time it takes the expansion wave to travel from $s = s_{exp}$ to the lowermost plane of the layer, $s = 0$.

Clearly, when the expansion wave passes the upper parts of the layer (corresponding to $s_{exp} \approx M$) they are subjected to larger pressure and hence yield larger Δu. On the other hand, by the time of arrival of the expansion wave at the lower parts (with s_{exp} close to 0) they are almost 'cold' and, hence do not contribute to Δu_m, and hence to Δu, i.e. $\Delta u(0) \approx 0$. This leads to the velocity gradient $\partial \Delta u/\partial s$ across the layer, which cause its expansion. We will replace $\Delta u(s)$ by a linear function

$$\Delta u(s_{exp}, t) = \overline{\frac{\partial \Delta u}{\partial s}} s_{exp},$$

wherein $\overline{\partial \Delta u/\partial s}$ is the average velocity gradient, which can be expressed by integrating both sides of the above equation:

$$\overline{\frac{\partial \Delta u}{\partial s}} = \frac{2}{M^2} \int_0^M \Delta u(s_{exp}, t)\, \mathrm{d}s_{exp}. \tag{41}$$

We will further evaluate the integral in (41). Towards this goal note that in accordance with the definition of the speed of sound, s_{exp} is governed by the following equation:

$$\frac{\mathrm{d}s_{exp}}{\mathrm{d}t\rho_m} = -a(s_{exp}, t), \tag{42}$$

and the initial condition

$$s_{exp}(t_{sh}) = M. \tag{43}$$

Using (27), (30*d*) and (38*a*) one can write

$$\tilde{t} = t - t'_m - \frac{s}{D_L} \approx t - t'_m - \frac{s\Delta_0}{g\tau\rho_m}, \tag{44a}$$

and (37) may be rewritten in the form:

$$P^{(-1)}(t, s) = P_0 \left[1 + \frac{C(e)}{\sqrt{2}} \left(\frac{(t - t'_m) g\tau}{\Delta_0 \sigma} - \frac{s}{\rho_m \sigma} \right) \right]^{-2}. \tag{44b}$$

Using this equation together with equations of state (16) and (21) for the speed of expansion wave, equation (42) may be rewritten in the form

$$\frac{2\sqrt{6}}{C(e)} \sigma\rho_m \frac{\mathrm{d}(1/a)}{\mathrm{d}s_{exp}} = -\frac{1}{a} - \frac{\Delta_0}{g\tau}. \tag{45}$$

This should be solved subject to the initial condition (43), which with the help of (16), (44*b*) takes the form

$$a(M) = \sqrt{3}\, g\tau/\Delta_0. \tag{46}$$

Problem (45), (46) has the following solution

$$a(s_{exp}) = \frac{g\tau}{\Delta_0} \left[\left(1 + \frac{1}{\sqrt{3}} \right) \mathrm{e}^{\kappa(M - s_{exp})} - 1 \right]^{-1}, \tag{47a}$$

wherein the coefficient κ is

$$\kappa = C(e)/(2\sqrt{6}\sigma\rho_m). \tag{47b}$$

One can see from (46), (47*a*) that shortly after $t = t_{sh}$ when the shock wave arrives at the top of layer ($s_{exp} = M$), the speed of sound is comparable to the kinematic shock wave speed $D = D_L/\rho_m$ with D_L given by (38*a*). However, when the expansion wave reaches the layer bottom ($s_{exp} = 0$), its speed of propagation is much less than D (by a small factor $\exp(-\kappa M)$).

Using (47), (21) and (40*a–c*) one can calculate

$$\Delta u_m(s_{exp}) = \frac{g\tau}{\sqrt{3}}\left[\left(1+\frac{1}{\sqrt{3}}\right)e^{\kappa(M-s_{exp})}-1\right]^{-1}, \tag{48a}$$

$$t_{exp}(s_{exp}) = \frac{\Delta_0}{g\tau\kappa\rho_m}\left[\left(1+\frac{1}{\sqrt{3}}\right)(e^{\kappa(M-s_{exp})}-1)-\kappa(M-s_{exp})\right]. \tag{48b}$$

When the expansion wave reaches the bottom of the layer ($s = 0$) it detaches from the vessel and the free flight begins. During this stage gravitation acts in the same manner upon all the granules and, hence, the velocity gradients do not change. We therefore calculate the average velocity gradient at the moment of detachment, $t_{exp}(0)$. Calculations according to (40), (41) yield

$$\overline{\frac{\partial \Delta u}{\partial s}} = \frac{2g\tau}{M}\left[f(H)-\frac{\Delta_0 h_m}{g\tau^2}q(H)\right], \tag{49}$$

where

$$f(H) = \frac{1}{H}\ln(1+\sqrt{3}-\sqrt{3}\,e^{-H/\sqrt{3}}), \tag{50a}$$

$$q(H) = \frac{1}{H}\left[\left(1+\frac{1}{\sqrt{3}}\right)(e^{H}-1)-H\right]-\frac{1}{H^2}\left[\left(1+\frac{1}{\sqrt{3}}\right)(e^{H}-1-H)-\frac{H^2}{2}\right], \tag{50b}$$

and parameter H is given by

$$H = C(e)\,h_m/(2\sqrt{2\sigma}). \tag{51}$$

On the other hand, the spatial distribution of the velocity across the layer at time t_d may be determined from purely kinematic considerations by substituting (44*a*) into (31*b*):

$$u^{(0)} \approx A\omega\cos(\omega t_d)-g(t-t'_m-t_c-s/D_L), \tag{52}$$

valid during the free-flight stage. This solution predicts an average velocity gradient in the form

$$\overline{\frac{\partial u}{\partial s}} = \frac{\partial u^{(0)}}{\partial s} \approx \frac{g}{D_L}. \tag{53}$$

This velocity gradient was calculated from purely kinematic considerations, i.e. application of the plastic-body periodic motion combined with the shock wave kinematics. It should be equal to the velocity gradient given by (49), calculated by the energy conservation principle. This assumption leads to the following relation:

$$\overline{\frac{\partial \Delta u}{\partial s}} = \overline{\frac{\partial u}{\partial s}}, \tag{54}$$

which in combination with (49), (50*a*, *b*) and (53) yields the following expression for Δ_0:

$$\Delta_0 = k(H)\,(A\omega)^2/(gh_m), \tag{55a}$$

where
$$k(H) = \frac{f(H)}{\frac{1}{2} + q(H)}. \tag{55b}$$

Using (38*b*), one obtains the mass speed D_L of the shock front

$$D_L = \frac{2}{k(H)} \frac{gM}{A\omega}. \tag{56}$$

The time t_{sh} of propagation of the shock wave through the layer with mass per unit area M is

$$t_{sh} = \frac{k(H)}{2} \frac{A\omega}{g}. \tag{57}$$

We will also estimate the average granular pressure, $\bar{P}$, in the granular layer:

$$\bar{P} = \frac{1}{M} \int_0^M \langle P \rangle \, \mathrm{d}s, \quad \text{with} \quad \langle P \rangle = \frac{1}{\tau} \int_0^\tau P(t, s) \, \mathrm{d}\tilde{t}. \tag{58a, b}$$

This may be done by integrating (32*c*) from $\tilde{t} = 0$ to τ together with conditions (29*b*, *c*)

$$\frac{\mathrm{d}}{\mathrm{d}s} \langle P^{(0)} \rangle = -g. \tag{59}$$

Integrating this equation over the layer together with condition $P^{(0)} = 0$ for $s = M$, one obtains

$$\bar{P} \approx \overline{P^{(0)}} = Mg/2. \tag{60}$$

We note that the above result is exact, since it may be directly obtained from (23*b*) and condition (25*b*) without expanding P by (30*c*).

Now we can calculate the average value $\bar{\Delta}$ of the dimensionless density Δ, given by (35*b*) with $u^{(0)}(t)$ and $D_L^{(-1)}$ represented by (31) and (38*a*). These calculations may be simplified by bearing in mind that Δ changes insignificantly during the contact period, and changes linearly during the free flight. Accordingly, one obtains using (30*a*) and (55):

$$\bar{\Delta} = \tfrac{3}{2}\Delta_0 = \tfrac{3}{2} k(H) (A\omega)^2 / g h_m. \tag{61}$$

Analysing (61), one can see that one way to expand the layer (increase $\bar{\Delta}$) is to decrease the height h_m, which was done by Bachmann (1940). Another way to increase $\bar{\Delta}$ is to increase the maximum speed of wall oscillations, e.g. $A\omega$, which was observed in the experimental part of this study.

In order to obtain the average value $\bar{E}$ of the particle random-motion kinetic energy, integrate both sides of (16) over the layer mass and the time period. This together with (60) and the facts that $\Delta^{(1)}(\tilde{t}) \approx \Delta_0 = \text{const.}$ during the contact period and $E = 0$ during the free flight, yields

$$\bar{E} = \tfrac{1}{4} mg h_m \Delta_0. \tag{62}$$

This value may be compared with the initial energy E_0 supplied to the particles, which is by virtue of (16) and (38*b*)

$$E_0 = \frac{P_0 m}{2\rho_M} \Delta_0 = 2mA^2\omega^2. \tag{63}$$

Equations (62), (63) combined with (61) lead to

$$\bar{E}/E_0 = \tfrac{1}{8} k(H). \tag{64}$$

From this expression it is clear that $k(H)$ may be interpreted as a coefficient characterizing kinetic energy losses within vibrated layers with respect to the kinetic energy supplied by the wall. This coefficient depends on the dimensionless complex H, given by (51), which is proportional to the number of monolayers h_m/σ and the inelasticity factor $(1-e^2)$.

Formulae (56) and (61) imply that the average vibrational state properties are governed by the dimensionless parameter

$$V = A\omega/(gh_m)^{1/2}, \tag{65}$$

in terms of which one can write

$$\bar{\Delta} = \tfrac{3}{2}k(H)V^2, \quad \frac{D_L}{\rho_m(h_m g)^{1/2}} = \frac{2}{k(H)}\frac{1}{V}, \quad \frac{\bar{E}}{mgh_m} = \frac{k(H)}{4}V^2. \tag{66a–c}$$

These relationships constitute our main result which will be analysed in the following section.

5. Discussion

Formulae (66*a–c*) are applicable to the collisional regime of vibrofluidized layers. Accordingly, they contrast with the results obtained in the treatments of Bachmann (1940), Kroll (1954), Gray & Rhodes (1972), Gutman (1976), Erdèsz & Mujumdar (1989), and Clement & Rajchenbach (1991), where the major part of the layer moved in the plastic body regime. In these studies not more than about five upper monolayers were fluidized. Estimates show that in these regimes parameter V is small, i.e. of order 0.1 or less. However, in the collisional regimes investigated here $V \sim 1$ (see table 2 below), which enabled full vibrofluidization of the layers at least for regimes characterized by (12*a*, *b*).

The solution obtained in the previous section supports the general scaling relations assumed in expansions (30*a–e*). In particular, one can see from (30*a*, *d*) that $u = O(1) \ll D = O(\Delta_0^{-1})$. This is also supported by the experimental data, which show that for the vibrational regimes used here $D \gg u \sim A\omega$ (see table 2 below).

Our model is based on experimental observations and basically differs from the model proposed by Haff (1983), who disregarded the wave propagation process in vibrated layers. He postulated, rather, that the particle kinetic energy in vibrated granular layers is transferred by 'conduction'. This assumption is physically non-plausible, since the oscillating wall cannot contribute to the granular kinetic energy of random motion without creating a (vertical) averaged hydrodynamic velocity. Hence, wall-layer interactions inevitably lead to the formation of shock waves. Haff's model, thus, accounts for the higher-order effects and disregards the primary (wave propagation) mechanism governing energy transfer in vibrated granular layers.

Equation (66*b*) predicts that the shock wave speed is inversely proportional to V. In fact neither direct measurements nor calculations of the speed of shock wave propagation in bulk materials have been performed. Gray & Rhodes (1972), however, reported that a stress wave propagated through their bed composed of solid particles with a velocity of about 150 m s^{-1}. Such a wave takes about 1 ms to reach the upper surface of a bed of 15 cm thickness. Bearing in mind this fact together with (56), (61) it is possible to estimate the average deviation $\bar{\Delta}$ from the maximum particle concentration in Gray & Rhodes' experiments. Taking $f = 50$ Hz, $\Gamma = 4$, one obtains the maximum wall velocity $u_{max} = A\omega = 0.127$ m s^{-1} and $\bar{\Delta} \sim 0.0034$. Such small

No.	Source of the data	A (cm)	f (Hz)	$\Gamma = A\omega^2/g$	h_m/σ monolayers	n (cm^{-2})	Δ	$V = A\omega/(gh_m)^{1/2}$	k	D (m s^{-1})	H
1	Figure 2(*a*)	0	0	0	15	4.2	0	—	—	—	—
2	Figure 2(*b*)	1	5	0.9	15	4.2	0	0.62	—	—	—
3	Figure 4(*a*)	3	5	2.7	15	3.4	0.19	1.25	0.122	20.5	3.47
4	Figure 4(*b*)	3	5	2.7	15	3.3	0.21	1.25	0.134	17.7	3.47
5	Figure 7	1	15	8.9	10	2.3	0.45	1.88	0.127	8.3	2.31
6	Figure 8	1	16	10.1	15	2.5	0.4	1.35	0.219	9.9	3.47
7		2	6	2.84	20	3.7	0.12	0.73	0.225	24.7	4.62
8	Gray & Rhodes	0.04	50	4	30	~ 4.2	0.0034	0.085	0.47	150	~ 2.1

TABLE 2. Particle concentration, Δ, and the energy coefficient k, calculated on the basis of the experimental data obtained for various vibrational states. For rows 3 and 4 averaged data are presented as a single experimental point in figure 13. Photographs from which the data for row 7 were obtained are not presented. Data for row 8 were calculated on the basis of the values of wave propagation velocity and shock wave propagation time, reported in Gray & Rhodes (1972), and under the assumption that only five upper monolayers are vibrofluidized.

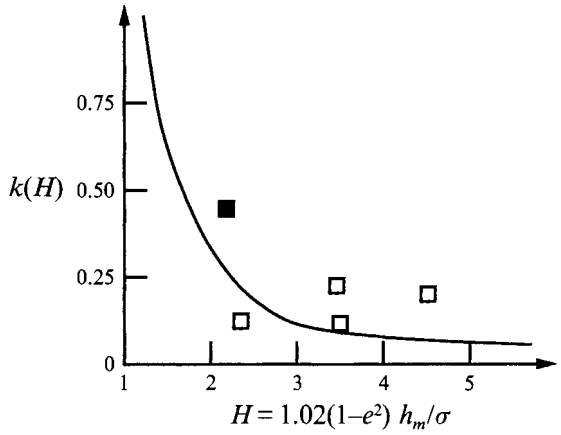

FIGURE 14. Comparison between theoretically calculated and experimentally measured kinetic energy loss coefficient: hollow symbols – present data; solid symbols – Gray & Rhodes (1972).

deviations from the maximum packing density practically cannot be measured. This justified their solid-body considerations of the layer motion.

5.1. *Testing of the collisional gas-like state model*

The vibrofluidized layer model given by (56), (61) was verified by using the experimental data presented in figures 2, 4, 7 and 8 to calculate the coefficient k appearing in these equations. Explicitly, control volumes were chosen in the above photographs, containing several hundreds of particles, for which the particle number concentrations were calculated. The results were used to calculate Δ by formula (15), which values were used as estimates for the average deviation $\bar{\Delta}$ from the maximum packing density. Then (61) was solved to obtain the value of k for given A, f and h_m. Independently, the coefficient H was calculated from (51) using the restitution coefficient $e = 0.88$, measured for the glass balls.

The results of the calculations are summarized in table 2. It can be seen that vibrational excitation of granular layers in the non-detaching regime does not lead to appreciable changes of average particle concentration (see rows 1 and 2 of the table). The value $n = 4.2\ \text{cm}^{-2}$, obtained from figure 2(a, b) was chosen as an estimate for the maximum packing density of the considered system of spheres.

The data taken from Gray & Rhodes (1972) are also listed in the table, together with the corresponding value of k. This was calculated using their data $D = 150\ \text{m s}^{-1}$ and assuming $h_m = 5\sigma$, i.e. only five upper monolayers are fluidized as was observed by Bachmann (1940) for regimes characterized by low V and high Γ. The shock wave velocities in our experiments (with much higher V) are about ten times less than those reported by Gray & Rhodes (1972). Alternatively, this difference stems from the lower particle concentration in our experiments.

The values of k calculated from the experimental data are shown in figure 14, where the theoretical $k(H)$ curve is given by (55b), (50a, b). The data of Gray & Rhodes (1972) are also plotted. One can see that the experimental results fit the model predictions well. In particular, one can note that data collected for the solid-like regimes satisfactorily agree with the calculations performed for the collisional model. This underlies the dual nature of the solid-like vibrational regime, which on the one hand yields solid-body kinematics, and on the other hand reveals internal energy transfer processes, well correlated by the gas-like model. Additional support of the

present model is given in Part 3 of this series (Goldshtein, Shapiro & Gutfinger 1995), where the energy transfer coefficient $k(H)$ is compared with the corresponding result obtained from an exact analytical solution of the shock wave propagation problem in a semi-infinite granular layer.

The shock wave shown in figure 7 is seen to propagate into a *cold* granular gas. The speed D of the shock front may be estimated from table 2 and is of order 10 m s^{-1}. This is clearly much more than the speed of sound a in the cold granular layer, since the kinetic energy E governing the value of a (see (21)) is very small. This statement may be supported by figure 7 (where the granules lying above the front are almost stagnant) and by the proposed model, which predicts fast exponential decay of a with time (see (47a) and the explanations which follow it). Note that the ratio a/D is given by $\exp(-\kappa M) = \exp(-H) \ll 1$ (see table 2 for the values of H).

The particle number concentrations observed in figures 7 and 8 are relatively large ($\Delta = 0.4$ and 0.45, see table 2). For such number concentrations the assumptions underlying the model developed in the previous section, in particular the assumption $\Delta \ll 1$ and equation of state (16), are not justifiable. This can partially explain the difference between the experimental and calculational values of k for these regimes. Another possible reason is that the values of n evaluated from the photographs are instantaneous quantities and, generally, differ from the comparable time-averaged quantities, appearing in (56), (61). Therefore, the results of calculations in table 2 should be viewed only as estimates. Bearing this in mind the agreement shown in figure 14 is surprisingly good.

5.2. '*Visualization*' *of the shock front by photographing systems*

We will discuss here the choice of the exposure time for photographing the shock front propagating through vibrated granular layers. In all experiments we observed that the particle number density changed insignificantly during the vibrational period. As such, the dimensionless difference $[\![\Delta]\!]$ between the particle number concentrations in front of and behind the shock front is usually small and the front's position may be identified only by the difference between the particle velocities in the 'cold' (before the front) and the 'hot' parts of the layer. This difference is visualized in the photograph by observing the images of 'hot' (moving) particles as ellipses (see e.g. figure 7), while the 'cold' particles appear as circles. In order to obtain a clear ellipse-like image of a particle of diameter σ and moving with velocity v, one should choose the exposure time t_e of the photographing system as

$$t_e \sim \sigma/v. \tag{67}$$

On the other hand, the exposure time should be much less than the time t_{sh} during which the shock front travels across the layer:

$$t_e < t_{sh}. \tag{68}$$

Using in (67) particle's velocity $v = (2E_0/m)^{1/2} = 2A\omega$ (see (63)), and employing (57) for t_{sh} together with (68), one obtains the following condition on t_e:

$$\frac{\sigma}{2A\omega} \sim t_e \ll k\frac{A\omega}{2g}. \tag{69}$$

It appears, thus, that the proper choice of the exposure time depends upon the vibrational regime and the particle size, but is independent of the particle's mass. Condition (69) may thus be used to rationally design the photographing or high-speed videorecording system for investigation of wavy regimes of vibrofluidized granular layers.

The data appearing in the third and fourth rows of table 2 correspond to different phases of the same vibrational regime of figure 4(*a*, *b*). It may be seen that neither Δ nor k exhibits significant variations and, hence, for this regime one may take $\bar{\Delta} = 0.2$ and $k = 0.112$. One can use these values to calculate according to (57) the characteristic travelling time of the shock wave, as $t_{sh} = 0.0018$ s. This time is less than the minimal exposure time $t_e \sim \sigma/(2A\omega) = 0.027$ s of the photographing system given by (67). It is, therefore, clear why no shock waves can be registered by this optical method for the regime $A = 3$ cm, $f = 5$ Hz, corresponding to figure 4(*a*, *b*). For such vibrational regimes the above method of longitudinal wave visualization is inefficient. Therefore, in these cases a shorter exposure time $t_e = 1/14000$ s was employed, which enabled clear particle images to be obtained and facilitated measurement of the bulk density.

On the other hand, the shock wave can be easily observed on figure 7 where $t_{sh} = 0.0079$ s and $t_e = 0.004$ s. For such a large shock propagation time the front may be registered either by phase-independent video-photographing, from frame-by-frame observations, or from series of non-synchronized camera shots. Therefore, by choosing proper vibrational regimes (where the layer is well expanded and the shock wave speed is low), one can easily observe shock front propagation even with low-speed phase-independent videorecording.

5.3. *Granular kinetic energy within the vibrofluidized layer*

Formula (64) together with the values of $k(H)$ calculated from (55*b*) may be used to calculate average granular kinetic energy. These expressions show that the major part of the energy which the layer receives from the vessel is lost due to inelasticity of the particles collisions, even when the restitution coefficient is as high as 0.88. This estimation is an additional justification of the strong shock wave approximation (28) and the employment of the solid plastic body model for $t > t_c$, made in the previous section. As we have seen above, the estimates made for the vibrofluidized regimes summarized in table 2 lead to the conclusion that granular layers constitute rather 'cold' and 'dense' gases as compared with molecular gases. Nevertheless, high-amplitude and low-frequency vibrations yield much less dense layers than those characterized by the same dimensionless acceleration Γ, albeit vibrated with *low* amplitude and *high* frequency. Indeed, one can use (61) to see that for obtaining a particle concentration corresponding to $\bar{\Delta} = 0.2$ of the layer of particles with $e = 0.88$ and h_m, V as in row 3 of table 2, using frequency $f = 50$ Hz, one needs to achieve accelerations of about $\Gamma = 27$ (i.e. ten times larger than in the regime $A = 3$ cm, $f = 5$ Hz). It is clear that such large accelerations necessitate the application of very high power and significantly reduce the operational time of vibrational machines. Our results, therefore, may be used to design efficient vibrational machines for processing granular materials.

6. Concluding remarks

The collisional motion of vibrofluidized layers observed for granular layers vibrated with small frequency and large amplitude ($A \geqslant 0.5$ cm) is characterized by longitudinal shock and expansion waves. The former waves propagate within the layer with a speed exceeding that of small disturbances (speed of sound). The existence of both expansion and shock waves constitutes an inherent property of the collisional motion of vibrofluidized coarse granular materials. These waves serve as a mechanism sustaining the collisional gas-like regime of the particle motion.

The above regime differs markedly from the single plastic body behaviour observed

previously for layers composed of coarse granules and vibrated with small amplitudes and large frequencies.

In the liquid-like state transverse waves were observed which were shown to result from gravity-induced instabilities of the one-dimensional layer motion. The vibrational resonant frequencies calculated via the layer aspect ratio h_m/L are in a satisfactory agreement with the experimentally observed values.

An approximate model proposed for the collisional regime of the vibrofluidized layer motion yields scaling of the particle average vibrational state parameters via the dimensionless criterion $V = (A\omega)/(h_m g)^{1/2}$. The propagation speeds of shock and expansion waves, as well as the average values of the kinetic energy of particle random motion are expressed in terms of V and a dimensionless coefficient $k(H)$. The complex H was shown to depend upon the layer dimensionless thickness and particle restitution coefficient. Physically k characterizes total kinetic energy losses within the layer with respect to the energy supplied by the vibrating vessel. By analysing the particle number density shown on different photographs, the latter coefficient was calculated and found to agree with the values calculated from the model.

This research was supported by Technion V.P.R. Fund – Promotion of Sponsored Research Fund. The authors are grateful to Professor C. Campbell for a discussion on the subject of the paper and to Professor H. S. Herrmann and Dr S. Melin for providing a videofilm with computer simulations of the granular motion.

REFERENCES

AHMAD, K. & SMALLEY, I. J. 1973 Observation of particle segregation in a vibrated granular system. *Powder Technol.* **8**, 69–75.

ALDER, B. J. & HOOVER, W. G. 1968 Numerical statistical mechanics. In *Physics of Simple Liquids*, pp. 79–114. North-Holland.

BACHMANN, D. 1940 Verfahrensttechnik Z.V.D.I. Beiheft 2, 43, cited in the paper by Thomas *et al.* (1989).

BLEKHMAN, I. I. & DZHANELIDZE, D. G. 1964 *Vibrational Transport*. Moscow: Nauka (in Russian).

BUEVICH, YU. A., SUTKIN, S. V. & TETUKHIN, V. V. 1984 To the theory of magneto-fluidized bed. *Sov. Mag. Gidrod.* **4**, 3–11.

CAMPBELL, C. S. 1990 Rapid granular flows. *Ann. Rev. Fluid Mech.* **22**, 57–92.

CHAPMAN, S. & COWLING, T. G. 1970 *The Mathematical Theory of Non-Uniform Gases*, 3rd edn. Cambridge University Press.

CHLENOV, V. A. & MIKHAILOV, N. D. 1972 *Vibrofluidized Beds*. Moscow: Nauka (in Russian).

CLEMENT, E. & RAJCHENBACH, J. 1991 Fluidization of a bidimensional powder *Europhys. Lett.* **16**, 133–138.

COURANT, R. & FRIEDRICHS, K. O. 1948 *Supersonic Flow and Shock Waves*. Interscience.

DRAKE, T. G. 1990 Granular flow: physical experiments and their implication for microstructural theories. *J. Fluid Mech.* **225**, 121–152.

ERDÈSZ, K. & MUJUMDAR, A. S. 1989 Numerical investigation of a phenomenological model for vibrated fluidized beds. *Drying Technol.* **7**, 487–502.

ERDÈSZ, K. & NÈMETH, J. 1988 Methods of calculation of vibrational transport rate of granular material. *Powder Technol.* **55**, 161–170.

FAUVE, A., DOUADY, S. & LAROSHE, C. 1989 Collective behaviors of granular masses under vertical vibrations. *J. Physique Colloque* C3, **50** (3), 187–191.

GOLDSHTEIN, A. & SHAPIRO, M. 1995 Mechanics of collisional motion of granular materials. Part 1. General hydrodynamic equations. *J. Fluid Mech.* **282**, 75–114.

GOLDSHTEIN, A., SHAPIRO, M. & GUTFINGER, C. 1995 Mechanics of collisional motion of granular materials. Part 3. Self-similar shock-wave propagation. *J. Fluid Mech.* (submitted).

GRAY, W. A. & RHODES, G. T. 1972 Energy transfer during vibratory compaction of powders. *Powder Techn.* **6**, 271–281.

GUTMAN, I. 1968 *Industrial Uses of Mechanical Vibrations.* London: Business Books.

GUTMAN, R. G. 1976 Vibrated beds of powders. Part I: A theoretical model for the vibrated bed. *Trans. Inst. Chem. Engrs* **54**, 174–183.

HAFF, P. K. 1983 Grain flow as a fluid-mechanical phenomenon. *J. Fluid Mech.* **134**, 401–430.

HOMSY, G. M., JACKSON, R. & GRACE, J. R. 1992 Report of a symposium on mechanics of fluidized beds. *J. Fluid Mech.* **236**, 447–495.

JENKINS, J. T. & SAVAGE, S. B. 1983 A theory for rapid flow of identical, smooth, nearly elastic, spherical particles. *J. Fluid Mech.* **130**, 187–202.

KROLL, W. 1954 Über das Verhalten von Schüttgut in Lotrecht Schwingenden Gefäben. *Forshung* **20**, 2–15.

LANDAU, L. & LIFSHITZ, E. 1987 *Fluid Mechanics.* Pergamon.

MEAKIN, P. & SKJELTORP, A. T. 1993 Application of experimental and numerical models to the physics of multiparticle systems. *Adv. Phys.* **42**, 1–127.

MOODY, D. M. 1990 Unsteady expansion of an ideal gas into a vacuum. *J. Fluid Mech.* **214**, 455–468.

NIGMATULLIN, R. I. 1978 *Fundamentals of the Mechanics of Heterogeneous Media.* Moscow: Nauka (in Russian).

RASKIN, KH. I. 1975 Application of the methods of physical kinetics to problems of vibrated granular media. *Dokl. Acad. Nauk SSSR* **220**, 54–57.

ROBERTS, A. W. 1984 *Handbook of Powder Science and Technology.* Van Nostrand Reinhold.

SAVAGE, S. B. 1984 The mechanics of rapid granular flows. *Adv. Appl. Mech.* **24**, 289–366.

SAVAGE, S. B. 1988 Streaming motions in a bed of vibrationally fluidized dry materials. *J. Fluid Mech.* **194**, 457–478.

THOMAS, B., LIU, Y. A., CHAN, R. & SQUIRES, A. M. 1987 A method of observing phase dependent phenomena in cyclic systems: Application to study of dynamic of vibrated bed of granular solids. *Powder Technol.* **52**, 77–92.

THOMAS, B., MASON, M. O., LIU, Y. A. & SQUIRES, A. M. 1989 Identifying states in shallow vibrated beds. *Powder Technol.* **57**, 267–280.

THOMAS, B. & SQUIRES, A. M. 1989 Vibrated bed microreactors simulating catalytic fluid beds: A feasibility bed. In *Fluidization IV* (ed. J. R. Grace, L. W. Shemilt & M. A. Bergoughou) Alberta, Canada: Benif.